

**Department of Physics and Astronomy
Heidelberg University**

Bachelor Thesis in Physics
submitted by

Ian David Linnett

born in Frankfurt a.M. (Germany)

2025

First Sensor Capacitance Measurements of High-Voltage Monolithic Active Pixel Sensors for the LHCb Upgrade II Mighty Tracker

This Bachelor Thesis has been carried out by Ian David Linnett at the
Physikalisches Institut in Heidelberg
under the supervision of
Prof. Dr. Ulrich Uwer

Abstract

During Long Shutdown 4 of the LHC, the LHCb tracking system is foreseen to be substantially upgraded by replacing the Scintillating Fibre Tracker with the Mighty Tracker, enabling it to cope with the increased instantaneous luminosity at the interaction point. The new tracking detector will feature an outer section continuing to use scintillating fibres, while the inner section will be based on silicon pixel detectors, specifically HV-MAPS.

In this work, a method to measure the sensor capacitance is developed and applied to characterise the prototype sensor MightyPix1. The capacitance under varying bias voltages, temperatures and radiation fluences is analysed and used to derive the depletion depth and resistivity. For the unirradiated sensor, a resistivity of $(405 \pm 8) \Omega \text{ cm}$ is obtained, consistent with measurements of the manufacturer of $(369 \pm 21) \Omega \text{ cm}$. The resistivity and doping concentration are presented, and the behaviour at full depletion is analysed. Furthermore, the impact of non-ionising radiation on the sensor is studied, showing a decrease in doping concentration with increasing radiation levels and introducing a temperature dependence of the capacitance measurement.

Zusammenfassung

Während der vierten Wartungspause des LHC soll das LHCb Spurrekonstruktionssystem umfassend aufgerüstet werden, indem der Mighty Tracker den Szintillationsfaser-Detektor ersetzt, um den Anforderungen der erhöhten instantanen Luminosität am Interaktionspunkt gerecht zu werden. Der neue Subdetektor wird im äußeren Bereich weiterhin Szintillationsfasern verwenden, während der innere Bereich auf Silizium-Pixeldetektoren, insbesondere HV-MAPS, basieren wird.

In dieser Arbeit wird eine Methode zur Bestimmung der Sensorkapazität entwickelt und angewendet um den Prototyp-Sensor MightyPix1 zu charakterisieren. Die Kapazität unter verschiedenen Biasspannungen, Temperaturen und Bestrahlungsdosen wird analysiert und genutzt um die Verarmungstiefe und die Resistivität zu berechnen. Für den unbestrahlten Sensor ergibt sich eine Resistivität von $(405 \pm 8) \Omega \text{ cm}$, übereinstimmend mit Messungen des Herstellers mit $(369 \pm 21) \Omega \text{ cm}$. Die berechnete Resistivität und Dotierungskonzentration werden präsentiert und das Verhalten bei voller Verarmung analysiert. Zusätzlich wird der Einfluss nicht-ionisierender Strahlung auf den Sensor untersucht, wobei eine Abnahme der Dotierungskonzentration mit steigender Bestrahlungsdosis beobachtet wird und sich eine Temperaturabhängigkeit der Kapazitätsmessung zeigt.

Contents

1	Introduction	5
2	Physics at LHC	7
2.1	Standard Model	7
2.2	The LHCb Experiment	8
2.3	Tracker Upgrade	10
3	Particle Detection	11
3.1	Ionization	11
3.2	Bremsstrahlung	12
4	Pixel Sensors	15
4.1	Semiconductors	15
4.1.1	Doping	18
4.2	P-n-Junction	20
4.3	p-n-Junction as Particle Detector	22
4.4	Resistivity and Doping Concentration	23
4.5	IV-Curves	24
4.6	Radiation-effects	25
4.7	HV-MAPS	28
5	RC-Circuits	31
5.1	Plate capacitor	31
5.2	Capacitor behaviour in an AC	32
5.3	RC-Circuits	33
6	Experimental Setup	35
6.1	The MightyPix1 Sensor	35
6.2	Measurement Circuit	36
6.3	Set-up Validation	39
6.4	Measurement Procedure	41
6.5	Cooling Setup	42
7	Capacitance-Measurements	45
7.1	Sensor Model	45
7.2	Sensor Thickness	49
7.3	Measurements at lower temperatures	53
8	Irradiated sensors	57

9	Capacitance behaviour at low bias voltage	63
10	Conclusion and Outlook	69
10.1	Conclusion	69
10.2	Outlook	70
11	Appendix	75
.1	Silicon values	75
.2	Impedance and Phase-shift Fits	75
.3	Fit-Model Comparison at lower Temperatures	77
.4	Acknowledgments	78

1 Introduction

The Standard Model of particle physics (SM) is the currently leading theoretical framework in particle physics for describing the fundamental particles and their interactions. It allows the characterization and prediction of particle decay processes, including the most prominent prediction of the Higgs Boson [1], proposed to exist by Peter Higgs in the 1960's and detected at the LHC in 2012 [2]. Yet, the SM is not an all explaining theory, as there are several phenomena which the SM can not explain. The search for new physics necessitates larger and more precise experiments. The largest current experiments in particle physics are conducted at the Large Hadron Collider (LHC) at CERN, where protons are accelerated and collided at high energies. One of the experiments at the LHC is the LHCb detector. At LHCb, heavy quark decays are investigated, with the goal to get a better understanding of flavour changes and CP-violation.

During the upcoming Long Shutdown 4, the luminosity is supposed to be significantly increased. To cope with the resulting higher particle rates and radiation levels, the downstream-tracking detector needs to be upgraded. Currently, the Tracker consists of Scintillating Fibres (SciFi), but in order to cope with the high luminosity, the centre region near the beam pipe will be replaced by pixel detectors to form the Mighty Tracker. These pixel detectors have a higher radiation hardness and granularity which ensures high tracking efficiency, which would not be achievable with the SciFi. The proposed technology for the Pixel Sensors are **H**igh **V**oltage **M**onolithic **A**ctive **P**ixel **S**ensors (HV-MAPS). In addition to the radiation hardness and granularity, HV-MAPS are produced in conventional HV-CMOS processes, therefore they are cost effective. Each HV-MAPS consists of a pixel array, with each pixel containing an n-well. When a charged particles ionizes the detector material, the drift of the electrons in the electric field induces a signal in the readout electrode, which houses in-pixel electronics. The monolithic structure results in a lower material budget for the sensor.

In this thesis, the bulk material is investigated using capacitance-voltage (CV) measurements. The active detection volume of the sensor is dependent on the voltage applied as well as the material properties. As the geometry of this volume has a similar structure to a plate capacitor, the capacity can be measured and used to calculate material properties such as the doping concentration and depletion depth. These characteristics are studied for varying irradiation doses and sensor thicknesses.

This thesis presents a systematic study of the capacitance-voltage behaviour of HV-MAPS under varying conditions, with the aim of enhancing the general understanding of depletion. For this, the different setups and the sensor used in this thesis are introduced and validated. The general model for describing the sensor is investigated which is then used to have a look at the CV-characteristics of the unirradiated sensors. Here, two different thicknesses are analysed, in order to see the general behaviour of the capacitance as well as complete depletion effects. This is followed by a study of CV-curves of irradiated sensors at

different temperatures, aimed at understanding the nature and extent of radiation-induced damage in the sensor. Last, the capacitance behaviour at low bias voltage is investigated. Finally there is a summary of the measurements together with a conclusion of what can be learned from the CV-curves, as well as what can still be improved to have a better understanding of distinct effects visible in the CV-characteristic.

2 Physics at LHC

2.1 Standard Model

The Standard Model of particle physics (SM) is a theory describing particles and their interactions. The dominant interactions are governed by three of the four forces: the electromagnetic force, the weak force and the strong force. The fourth force, gravitation, is not of importance for particles at current energies as the influence is minimal due to the low mass of particles.

The SM classifies fundamental particles into two main groups: fermions, which constitute matter, and bosons, which mediate forces. Fermions are further divided into leptons and quarks, both being particles with half-integer spin values obeying the Pauli exclusion principle. Leptons and quarks are further divided into three generations, with each generation containing two particles of different flavour. Every fermion has a corresponding antiparticle, identical in mass and spin but with opposite charge, denoted by a bar (e.g. $\bar{\mu}$ for the antimuon). This leads to a total of 12 particles and 12 antiparticles. All known particles, along with their mass, spin, and charge, are presented in Figure 1.






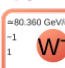
Standard Model of Elementary Particles											
three generations of matter (elementary fermions)						three generations of antimatter (elementary antifermions)			interactions / force carriers (elementary bosons)		
I		II		III		I		II		III	
mass charge spin	$\approx 2.2 \text{ MeV}/c^2$ $\frac{2}{3}$ $\frac{1}{2}$	$\approx 1.28 \text{ GeV}/c^2$ $\frac{2}{3}$ $\frac{1}{2}$	$\approx 173.1 \text{ GeV}/c^2$ $\frac{2}{3}$ $\frac{1}{2}$	$\approx 2.2 \text{ MeV}/c^2$ $-\frac{2}{3}$ $\frac{1}{2}$	$\approx 1.28 \text{ GeV}/c^2$ $-\frac{2}{3}$ $\frac{1}{2}$	$\approx 173.1 \text{ GeV}/c^2$ $-\frac{2}{3}$ $\frac{1}{2}$	0 0 1		$\approx 124.97 \text{ GeV}/c^2$ 0 0 0		
	u up	c charm	t top	\bar{u} antiup	\bar{c} anticharm	\bar{t} antitop	g gluon	H higgs			
	$\approx 4.7 \text{ MeV}/c^2$ $-\frac{1}{3}$ $\frac{1}{2}$	$\approx 96 \text{ MeV}/c^2$ $-\frac{1}{3}$ $\frac{1}{2}$	$\approx 4.18 \text{ GeV}/c^2$ $-\frac{1}{3}$ $\frac{1}{2}$	$\approx 4.7 \text{ MeV}/c^2$ $\frac{1}{3}$ $\frac{1}{2}$	$\approx 96 \text{ MeV}/c^2$ $\frac{1}{3}$ $\frac{1}{2}$	$\approx 4.18 \text{ GeV}/c^2$ $\frac{1}{3}$ $\frac{1}{2}$	0 0 1				
	d down	s strange	b bottom	\bar{d} antidown	\bar{s} antistrange	\bar{b} antibottom	γ photon				
QUARKS	$\approx 0.511 \text{ MeV}/c^2$ -1 $\frac{1}{2}$	$\approx 105.66 \text{ MeV}/c^2$ -1 $\frac{1}{2}$	$\approx 1.7768 \text{ GeV}/c^2$ -1 $\frac{1}{2}$	$\approx 0.511 \text{ MeV}/c^2$ 1 $\frac{1}{2}$	$\approx 105.66 \text{ MeV}/c^2$ 1 $\frac{1}{2}$	$\approx 1.7768 \text{ GeV}/c^2$ 1 $\frac{1}{2}$	$\approx 91.19 \text{ GeV}/c^2$ 0 0 1				
	e electron	μ muon	τ tau	e^+ positron	$\bar{\mu}$ antimuon	$\bar{\tau}$ antitau	Z ⁰ boson				
	$< 2.2 \text{ eV}/c^2$ 0 $\frac{1}{2}$	$< 0.17 \text{ MeV}/c^2$ 0 $\frac{1}{2}$	$< 18.2 \text{ MeV}/c^2$ 0 $\frac{1}{2}$	$< 2.2 \text{ eV}/c^2$ 0 $\frac{1}{2}$	$< 0.17 \text{ MeV}/c^2$ 0 $\frac{1}{2}$	$< 18.2 \text{ MeV}/c^2$ 0 $\frac{1}{2}$	$\approx 80.360 \text{ GeV}/c^2$ 1 1		$\approx 80.360 \text{ GeV}/c^2$ -1 1		
	ν_e electron neutrino	ν_μ muon neutrino	ν_τ tau neutrino	$\bar{\nu}_e$ electron antineutrino	$\bar{\nu}_\mu$ muon antineutrino	$\bar{\nu}_\tau$ tau antineutrino	W ⁺ boson	W ⁻ boson			
LEPTONS						GAUGE BOSONS VECTOR BOSONS			SCALAR BOSONS		

Figure 1: Overview of the elementary particles in the Standard Model, including fermions (quarks and leptons) and bosons (force carriers) [3].

Additionally, the Higgs boson is included in the Standard Model as the quantum excitation of the Higgs field, which is responsible for giving mass to the fundamental particles. Through their interaction with the Higgs field, particles gain mass proportional to the coupling to the higgs field. Its discovery at the LHC at 2012 confirmed a central aspect of the Standard Model [1].

The interactions in the SM are mediated by the bosons. Each boson is mediating one force:

the photon mediates the electromagnetic force, the gluon mediates the strong interaction and the W^\pm and Z^0 bosons mediate the weak interaction. In the weak interaction, flavour changes are possible in an interaction with a W-boson. These changes are described by the Cabibbo-Kobayashi-Maskawa (CKM) Matrix, parametrised by three mixing angles and one complex phase. This phase allows CP-violation.

With LHCb, transition probabilities of an up quark or a charm quark to a bottom quark - corresponding to the CKM matrix elements V_{ub} and V_{cb} - can be measured, as well as the angles β and γ . These measurements serve to test the Standard Model and may provide indications for physics beyond it.

2.2 The LHCb Experiment

The Large Hadron Collider beauty experiment (LHCb) is one of the four major experiments at the Large Hadron Collider. Its purpose is to improve the understanding of CP violation along with the decays of b and c hadrons. The detector is a single-arm forward spectrometer along the beam line, specifically designed to detect the particles of the b-hadron decay. It is located at one of the interaction points of the protons in the 27 km long proton beam at CERN. The detector itself consists of several subdetectors aligned one after another along the beam pipe.

The first subdetector is the Vertex Locator (VELO). It is located around the interaction point of the protons and it measures the trajectory of the particles right after the interaction in order to detect primary and secondary vertices. Heavy particles such as the b-hadron have a longer lifetime and thus decay after a short distance. The VELO is at a distance of 5.1 mm to the collision point [4]. Tracking in the VELO is performed through hybrid pixel sensors. In periods where there is no data collection, the VELO can be moved away from the beam-line in order to prevent radiation damage.

Next comes a Ring Imaging Cherenkov (RICH1), which is used to identify particles in low momentum tracks. The secondary particles created in the hadron decay are detected in the upstream tracking (UT) and in downstream tracking by Scintillating Fibre trackers, with upstream referring to the region before and downstream the region after a dipole magnet stationed along the beam. The maximum magnetic field in the centre of the magnet reaches 1.2 T [5]. The UT detects the position of short lived particles which do not traverse the magnet, as well as the entry angle of long living charged particles into the magnet. The UT itself is made up of 4 silicon strip detector layers, with the second and third layer being tilted in comparison to the outer layers for a higher resolution. Together with the VELO data, the track of a particle before the magnet is reconstructable.

Due to the charge, the trajectory of the particles is bent in the magnet. The curvature of the trajectory allows the momentum calculation of the particle. For this, the positions of the particles in the SciFi tracker are needed. The SciFi tracker consists of twelve

layers of scintillating fibres [6]. Particles passing through the SciFi lose energy by exciting molecules of the plastics to a higher energy state. When the excited molecules return to their ground state, the energy is emitted as scintillating light, which is shifted using wavelength shifting molecules and then guided through glass fibres to silicon photomultipliers (SiPMs). There, a signal for readout is created. After the SciFi, there is a second Cherenkov detector (RICH2) and then there are hadronic and electromagnetic calorimeters. These are used to measure the particles' energy. Each calorimeter consists of absorber material and scintillating material in alternating order. Electromagnetic showers are induced through the absorber material and then measured using the scintillating layers. The Calorimeters together with the Cherenkov detectors are used for the particle identification (PID). The last subdetector is the muon station, which is used for the identification and precise tracking of muons. A side view of the detector can be seen in Figure 2.

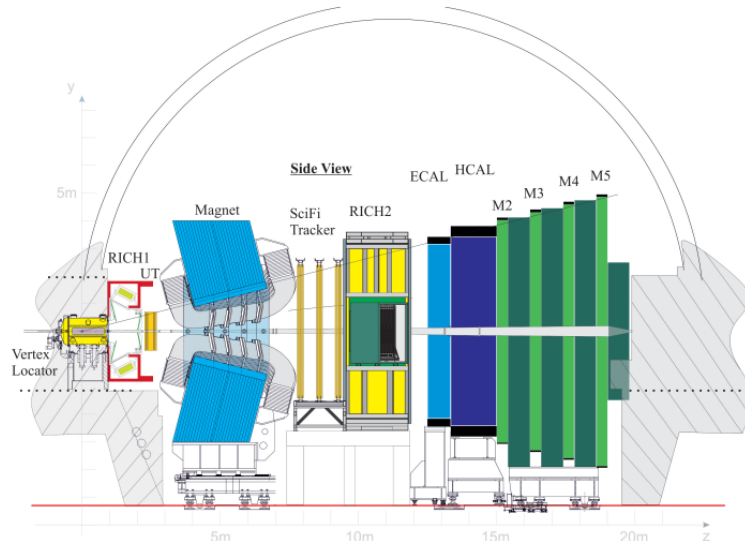


Figure 2: Schematic of the LHCb detector[7].

The detector covers the region of $2 < \eta < 5$, thus a very close range to the beam-line. This is motivated by the decays investigated in LHCb, which focus on heavy hadrons with low angle due to their high momentum.

The detectors detect signals at such a high rate that it is not possible to record. Thus, before saving the data, triggers are used to filter for interesting events. Since 2022, this triggering is performed solely software based. The High Level Trigger 1 (HLT1) filters the data rate according to the trajectory and a high transverse impulse. After the HLT1, the data rate is reduced to around 1 MHz. In the second trigger, the HLT2, a complete reconstruction of the event and particle identification is performed and filters based on physically interesting events are applied. The HLT2 decreases the rate to 10 – 30 kHz [8].

2.3 Tracker Upgrade

During the Long Shutdown 4 of the LHC, the LHCb detector is proposed to be upgraded to cope with the higher instantaneous luminosities of around $1.5 \times 10^{34} \text{ cm}^{-2} \text{ s}^{-1}$ [9]. The integrated luminosity is expected to increase to 300 fb^{-1} [9], thus the tracker needs to be able to detect more particles, but simultaneously be able to have a high efficiency after significant radiation exposure. Therefore, several upgrades will be performed on the detector until run 5. Firstly, the VELO will be renewed in order to be more radiation tolerant, as well as to get a higher resolution in space and time. The RICH 2 detector will be upgraded to the Time Of internally Reflected Cherenkov photons (TORCH) detector [10], which tracks the time of flight for particles between the interaction point and detector used for particle identification.

For the tracking, a higher granularity close to the beam is needed to cope with the high luminosity. As this can not be reached by the SciFi technology, the centre region will be replaced by silicon pixel detectors to form the new Mighty Tracker (MT). The MT will consist of twelve SciFi layers (MT-SciFi) and six pixel detectors layers (MT-Pixel) placed in a row. A frontal view of one of these stations can be seen in Figure 3. The proposed technology for the pixel sensors are HV-MAPS.

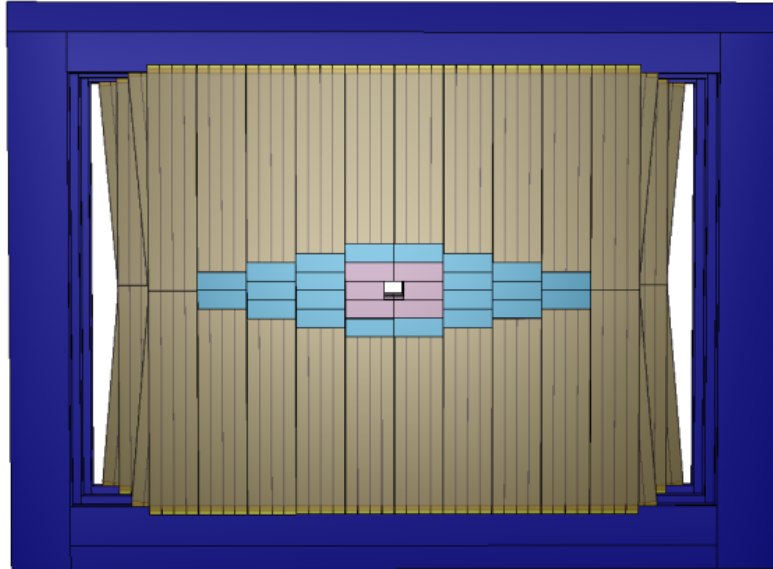


Figure 3: Schematic front view of the proposed Mighty Tracker. The central region (pink/blue) feature high granularity HV-MAPS, while the outer section features Scintillating Fibres. [11]

3 Particle Detection

When particles traverse material, they lose energy due to their interactions with matter. This energy-loss enables detection. In the context of the sensors used in this thesis, the charged particles primarily interact in two mechanisms: Ionization and Bremsstrahlung.

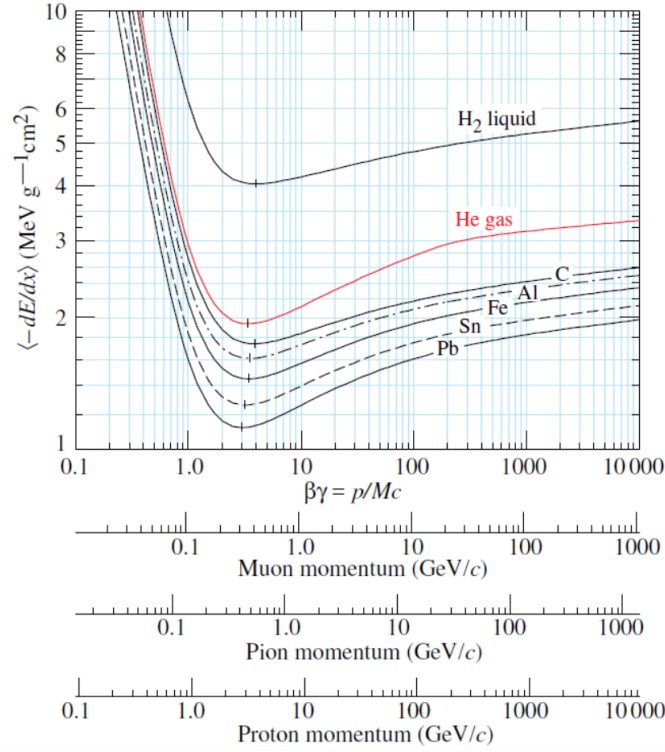
3.1 Ionization

When a highly energetic, charged particle moves through matter, it loses energy by interacting with the atoms of the material. This loss is primarily caused by collisions between the atoms in the matter and the incoming particle resulting in ionization and thus the emission of a (negatively charged) electron, creating a positively charged atom (an ion). The energy-loss depends on different statistical processes such as the probability of a collision and the energy that is transferred in the collision. Therefore it is only possible to define the mean energy-loss per distance $\left\langle \frac{dE}{dx} \right\rangle$. In a material with density ρ this energy loss can be described by the Bethe-Bloch-Formula [12]:

$$-\frac{1}{\rho} \left\langle \frac{dE}{dx} \right\rangle = \frac{K Z z^2}{A \beta^2} \cdot \left[\frac{1}{2} \ln \left(\frac{2m_e c^2 \beta^2 \gamma^2 E_{max}}{I^2} \right) - \beta^2 - \frac{\delta(\beta\gamma)}{2} \right] \quad (3.1.1)$$

Here, K is a constant ($K = 0.307 \text{ MeV cm}^2 \text{ mol}^{-1}$ [13]), Z is the charge number of the material ($Z=14$ for silicon) and z is the charge in units of the electron charge e of the incoming particle. Further constants are the mean excitation energy I ($I_{Si} \approx 173 \text{ eV}$ [14]) and the mass of the electron ($m_e = 0.511 \text{ MeV}$ [13]). The Bethe-Bloch-Formula is furthermore dependent on the relative velocity $\beta = \frac{v}{c}$ (c being the velocity of light) and the Lorentz-Factor $\gamma = \frac{1}{\sqrt{1-\beta^2}}$. Lastly, the energy loss is described by the maximum energy that can be transferred in a collision with an electron E_{max} . It is calculated from a two body collision in which the mass of one particle is significantly larger than the other, and is dependent on the mass and velocity of the interacting particle [13]. For high energies, the δ -term describes a density correction.

Theoretical values for different particles can be seen in Figure 4.

Figure 4: Mean energy-loss by ionization as a function of $\beta\gamma$. [13]

However, this formula is only valid for relativistic particles in the range of $0.1 \lesssim \beta\gamma \lesssim 1000$. For lower energies, the velocity of the particle is similar to the atomic electron velocity, leading to further interactions. At higher velocities, radiative effects gain importance [see [13], Chapter 34]. Both limits are dependent on the charge of the nucleus. Most importantly, this formula is only valid for heavy charged particles, therefore excluding electrons and positrons. The reason for this is the same mass of the incoming electrons with the ones in the material, rendering approximations such as the maximum energy loss invalid. For these two particles, the main energy loss occurs through Bremsstrahlung.

3.2 Bremsstrahlung

Bremsstrahlung in general refers to the radiation emitted by the acceleration or deceleration of a charged particle. In most cases however, it is describing the radiation of electrons (and equally positrons) in matter, which is the focus here.

As the electron traverses the matter, it can interact with the Coulomb field of a nucleus. The electron is diverted from its original trajectory and loses energy in form of a photon. If the energy of this photon is high enough, it can then interact with further atoms, potentially creating an electron-positron pair. If the energy of the primary electron as well as

the electron/positron created from the photon still carries enough energy, they can create another photon. This process continues as long as the energy of the particles retain sufficient energy. As the number of particles increases with every step, this process is called an *electromagnetic shower*. The total energy remains constant, while the energy for each particle is approximately halved over a characteristic distance. The average energy-loss per distance is described by:

$$\left| \frac{dE}{dx} \right|_{\text{brems}} \approx \frac{E_0}{X_0} \quad (3.2.1)$$

X_0 is the mean distance in which the electrons energy is reduced by $1/e$ and is material dependent ($X_{0,Si} = 9.37 \text{ cm}$).

4 Pixel Sensors

4.1 Semiconductors

Semiconductors are solid bodies whose conductivity lies in between that of insulators and that of conductors. For materials at the edges of the conductivity ranges, the definition by conductivity is not reasonable. A better definition is given by the band-structure of the different conductors.

The band-model is a model to describe the energy of the electrons in an atom-lattice. The eigenenergie of electrons is derived by the quantum mechanical wave function and is split in energy-bands, which electrons can occupy, and bandgaps, with no occupation. There are two bands: the *valence band*, which is the band containing electrons and the *conduction band*, the next higher band from the valence band. Only electrons in the conduction band act as charge carriers and therefore the conductivity of a material is dependent on the number of electrons in the conduction band. The conduction properties of a solid can be derived by examining the energy structure of its bands:

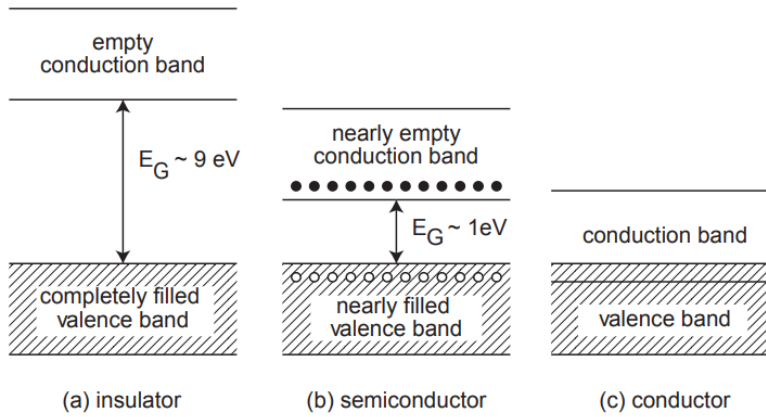


Figure 5: Schematic energy-band structure of insulators (a), semiconductors (b) and conductors (c). E_G is the energy distance of the band gap [12]

For conductors, the conduction and valence band overlap, allowing the valence electrons to move freely through the solid, acting as charge carriers. For semiconductors and insulators, there is a gap in between. In the case of insulators, the energy gap is too large for electrons to overcome through thermal excitation. Additionally, at the needed energy, the heat induced lattice vibrations result in a resistance that is too high for conductivity. These lattice vibrations also cause a negative temperature coefficient for conductors.

In semiconductors, however, the energy gap is relatively small, allowing some electrons to overcome the bandgap by thermal excitation. The energy is gained either by doping the

material (subsubsection 4.1.1) or heating. As the temperature increases, the mean energy of the electrons rises, resulting in a greater number of conduction electrons. Electrons that overcome the gap create a vacancy in the valance band, referred to as a *hole*, which can also move freely in the lattice and consequently contributes to the conductivity. The conductivity increase because of charge carriers is greater than the increase in resistance due to lattice vibrations, thus semiconductors have a positive temperature coefficient.

Typical semiconductors are made from elements of the fourth main group in the periodic table, as these form symmetric lattices. In the following, the focus lies on silicon, as this thesis focuses on silicon detectors. The energy of the bandgap of silicon is $E_G = 1.17 \text{ eV}$ at 0 K. This value is dependent on the distances of the atoms in the lattices and thus dependent on the temperature and pressure. For higher temperatures the distance between the atoms increases and thus the influence of the nucleus decreases slightly. Therefore at room-temperature the gap-energy decreases to $E_G = 1.12 \text{ eV}$.

As mentioned above, the electron transitioning from the valence band in to the conduction band creates a hole. This hole needs to be treated as a quasiparticle with positive charge, as its motion is induced by electrons hopping between adjacent states. The holes also contribute to the conductivity σ of the semiconductor:

$$\sigma = e \cdot (p\mu_p + n\mu_n) \quad (4.1.1)$$

Here, n and p are the charge carrier densities of the electrons and holes, and μ_i stands for the respective mobility.

As seen, the conductivity of a sensor is dependent on the charge carrier density. The first step to calculating the charge carrier density is to compute the charge carrier concentration $n(E)$, which gives the number of electrons per energy level.

The charge carrier concentration is proportional to the product of the density of states $Z(E)$ and their occupation probability $f(E)$. The number of states per volume and energy unit ($Z(E)$) is proportional to \sqrt{E} .

For electrons (and holes respectively) having spin of 1/2 affects their distribution over quantum energy states, since according to the Pauli principle, no two fermions can occupy the same set of quantum numbers. It can be implemented by the *Fermi-Dirac Distribution*:

$$f_n(E) = \frac{1}{\exp\left(\frac{E-E_f}{kT}\right) + 1} \quad (4.1.2)$$

E_f represents the Fermi Energy, T is the temperature in Kelvin and k the Boltzmann constant. The index n indicates negative charge carriers (electrons). For holes, E and E_f need to be swapped. For $T=0 \text{ K}$, the Fermi Energy is the energy up to which energy bands are completely occupied by electrons. For higher temperatures, the fermi energy is

the energy at which occupation by electrons equals 50%. This is roughly in the middle of the band gap.

The charge carrier density is the product of the density of states and occupation probability (see Figure 6).

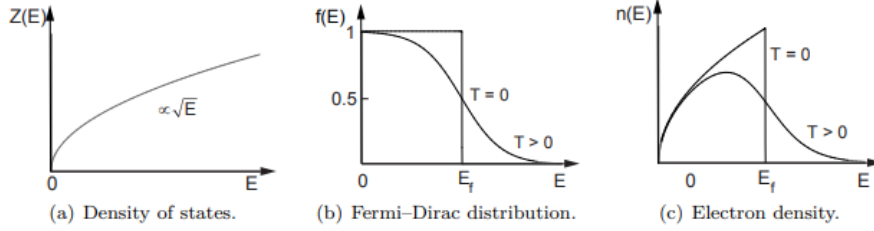


Figure 6: Density of states, fermi dirac distribution and electron density for semiconductors

In the context of semiconductors, the bandgap is accounted for by the step function Θ :

$$Z(E)dE = 4\pi \left(\frac{2m^*}{h^2} \right)^{\frac{3}{2}} \sqrt{E - E_C} \Theta(E - E_C) dE \quad (4.1.3)$$

$$Z(E)dE = 4\pi \left(\frac{2m^*}{h^2} \right)^{\frac{3}{2}} \sqrt{E_V - E} \Theta(E_V - E) dE \quad (4.1.4)$$

Here, m^* refers to the effective mass of the electron and the indices are referring to conduction band (C) and valence band (V).

As mentioned above, $n(E)dE$ (and $p(E)dE$) is the product of $Z(E)dE$ with the according Fermi-Dirac distribution in Equation 4.1.2. Since E_f is approximately in the middle of the bandgap and $(E - E_f) \gg kT$, the Fermi Dirac distribution simplifies to the Boltzmann distribution function:

$$f_n(E) = \frac{1}{\exp\left(\frac{E - E_f}{kT}\right) + 1} \approx e^{-\frac{E - E_f}{kT}} \quad (4.1.5)$$

This function decreases exponentially, therefore the number densities n and p (for electrons and holes) can be calculated by integrating over conduction band energies up to ∞ . The lower limit is given by the conduction band energy.

$$n = 2 \left(\frac{m_n^* kT}{2\pi\hbar^2} \right)^{\frac{3}{2}} \exp\left(-\frac{E_C - E_f}{kT}\right) = N_C \exp\left(-\frac{E_C - E_f}{kT}\right) \quad (4.1.6)$$

$$p = 2 \left(\frac{m_p^* kT}{2\pi\hbar^2} \right)^{\frac{3}{2}} \exp\left(-\frac{E_f - E_V}{kT}\right) = N_V \exp\left(-\frac{E_f - E_V}{kT}\right) \quad (4.1.7)$$

N_C and N_V being the effective densities of carriers in conduction and valence band, which calculate to

$$N_C = 2 \left(\frac{m_n^* kT}{2\pi\hbar^2} \right)^{\frac{3}{2}} \approx 3.05 \cdot 10^{19} \text{ cm}^{-3} \quad (4.1.8)$$

$$N_V = 2 \left(\frac{m_p^* kT}{2\pi\hbar^2} \right)^{\frac{3}{2}} \approx 2.55 \cdot 10^{19} \text{ cm}^{-3} \quad (4.1.9)$$

for silicon at 300K. The used effective masses for the electrons and holes ($m_n^* = 1.14m_e$ and $m_p^* = 1.01m_e$) are the averages over effective masses occurring due to the direction of the electron in the lattice [15].

The intrinsic charge carrier concentration n_i is defined as the number of free electrons and holes in a pure semiconductor at thermal equilibrium. At this state, the generation and recombination of electrons and holes are balanced, therefore the following relation holds:

$$n \cdot p = n_i^2 = \text{const} \quad (4.1.10)$$

This relationship also holds for semiconductors in which one charge carrier type occurs significantly more often than the other, such as in doped semiconductors (see subsection 4.1.1).

Using the formulas for n and p from Equation 4.1.6 and Equation 4.1.7, n_i computes to:

$$n_i = \left[N_C N_V \exp \left(-\frac{E_G}{kT} \right) \right]^{1/2} \propto T^{3/2} \cdot \exp \left(-\frac{E_G}{2kT} \right) \quad (4.1.11)$$

with $E_G = E_C - E_V$ being the energy of the bandgap.

4.1.1 Doping

With typical values for silicon (Table 4) and Equation 4.1.11, the intrinsic charge carrier density of silicon calculates to a value of $n_i \approx 1.01 \cdot 10^{10} \text{ cm}^{-3}$. This value is so low that it is not sensible to use it as a semiconductor.

To achieve higher electrical conductivity, the charge carrier concentration must be increased. This can be done by doping the silicon, meaning to add impurity atoms. Replacing a silicon atom by a pentavalent atom (such as phosphorus or arsenic) leads to an n-doped silicon semiconductor. This kind of doping introduces electrons as charge carriers, therefore creating a semiconductor with more electrons than holes. Respectively, replacing a silicon atom by a trivalent atom (such as boron or gallium) leads to a p-doped silicon semiconductor, a semiconductor with more holes than electrons [12]. Through doping, the number of free charge carriers available for conduction increases. A schematic with arsenic and boron as doping atoms can be seen in Figure 7.

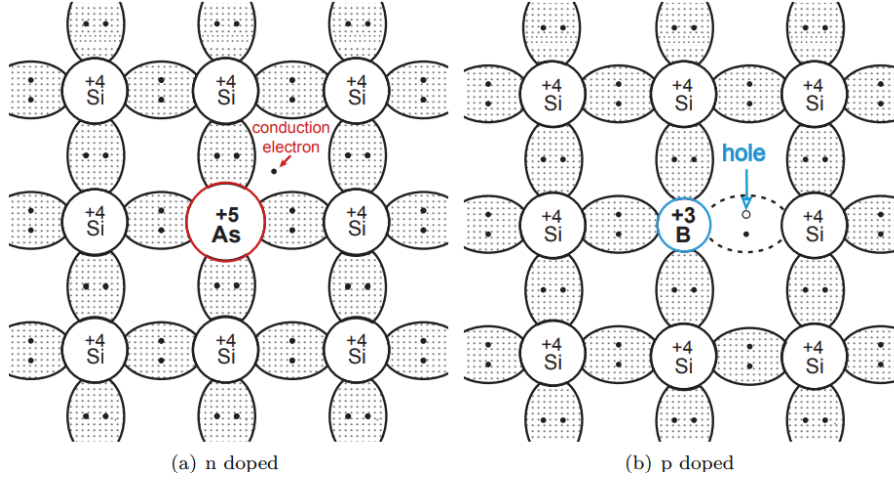


Figure 7: Schematic of the lattice in n-doped (a) and p-doped (b) silicon. [12]

The total charge of the semiconductors remains zero as added electrons come with a higher nucleus charge and vice versa.

This charge neutrality holds for each volume section, therefore charge density is defined by

$$\rho_c = e(n - p + N_D - N_A) = 0 \Rightarrow n - p = N_D - N_A \quad (4.1.12)$$

As before, n and p are the concentrations of electrons and holes and N_D and N_A resemble the concentrations of donor and acceptor atoms injected in the semiconductor.

As mentioned above, the equilibrium equation Equation 4.1.10 also holds for doped materials. Substituting the relation from Equation 4.1.12 in the equilibrium equation, the electron density for n-type semiconductor ($N_D \gg n_i \gg N_A$) calculates to

$$n_n = \frac{1}{2} \left(N_D - N_A + \sqrt{4n_i^2 + (N_D - N_A)^2} \right) \approx |N_D - N_A| \approx N_D \quad (4.1.13)$$

and the concentration of holes in a p-type semiconductor ($N_A \gg n_i \gg N_D$) calculates to

$$p_p = \frac{1}{2} \left(N_A - N_D + \sqrt{4n_i^2 + (N_D - N_A)^2} \right) \approx |N_A - N_D| \approx N_A \quad (4.1.14)$$

In the context of silicon sensors, the doping is typically on the order of $1 \times 10^{13} \text{ cm}^{-3}$. Thus, the approximation of $N_i \gg n_i$ is valid.

4.2 P-n-Junction

A p-n-junction is a fundamental semiconductor device formed by joining p-type and n-type materials, creating a diode that allows current to flow primarily in one direction. In order to understand the functioning of the diode, it is essential to examine what happens at the interface point.

As can be seen in Figure 8, for p-doped silicon, the Fermi level is near the valence band energy, while for n-doped silicon, the Fermi level is near the conduction band energy. This difference in energy leads to a *diffusion current* I_{diff} , and thus a diffusion of electrons from the n-doped silicon to the p-doped silicon [12]. Equivalently, the holes from the p-doped region diffuse to the n-doped region. Near the junction, the electrons and holes from the drift recombine, creating a region free of charge carriers, the depletion region. Since the non-depleted regions of the silicon now have less free charge carriers, but the same number of ionised atom-cores, they are not neutral. The p-doped region has a negative charge (loss of positive holes) and the n-doped region has a positive charge (loss of negative electrons). A schematic of the energy-bands in the p-n-junction can be seen in Figure 8.

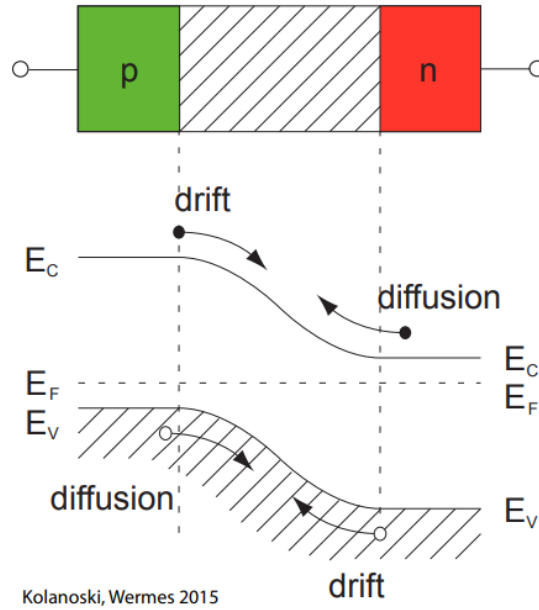


Figure 8: Energy-levels with electron and hole drift for a p-n-junction. [12]

Due to the charged non-depleted regions, an electric field in the depletion region acts as a force on the electrons and holes, inducing a drift current I_{drift} [16]. For electrons, this leads to a drift from the negative p-doped region to the positive n-doped region. For holes, this is exactly opposite. The movement of the charge carriers continues until an equilibrium between drift and diffusion is reached. The electric potential created by the

charge separation in the depletion region causes a gradual bending of the energy bands across the junction interface. However, the Fermi level remains the same due to it being defined by the occupation probability. These effects are also visible in Figure 8.

The effects are independent of direction. For simplicity, further calculations are all performed along the x-axis. In the depleted region, the charge density $\rho(x)$ is given by [17]:

$$\rho_c(x) = \begin{cases} -eN_A, & \text{for } -x_p < x < 0 \\ +eN_D & \text{for } 0 < x < x_n \end{cases} \quad (4.2.1)$$

Since the p-type and n-type semiconductor are neutral, the junction also has to be neutral. This is expressed in the neutrality condition, which holds for every further calculation:

$$N_A x_p = N_D x_n \quad (4.2.2)$$

With x_p being the edge of the p-doped region and x_n the edge of the n-doped region. From this, the Electrical field $E(x)$ can be calculated using the first Maxwell equation (Equation 4.2.3), which simplifies to Equation 4.2.4 in the one dimensional case.

$$\vec{\nabla} \vec{E} = \frac{\rho}{\epsilon_0} = -\nabla^2 \Phi \quad (4.2.3)$$

$$\frac{dE}{dx} = \frac{\rho}{\epsilon_0 \epsilon_r} \quad (4.2.4)$$

Since the electric field is zero for charge carrier free regions, we obtain the boundary conditions $E(-x_p) = E(x_n) = 0$. Solving the one dimensional Maxwell equation leads to:

$$E(x) = \begin{cases} \frac{-eN_A}{\epsilon_0 \epsilon_r} (x + x_p), & \text{for } -x_p < x < 0 \\ \frac{+eN_D}{\epsilon_0 \epsilon_r} (x - x_n) & \text{for } 0 < x < x_n \end{cases} \quad (4.2.5)$$

The electric field can be used to calculate the potential for the junction, from which the bias voltage V_{bi} across the depletion zone is obtained as the difference in potential between its boundaries.

$$V_{bi} = \phi_n - \phi_p = - \int_{-x_p}^{x_n} E(x) dx \quad (4.2.6)$$

$$= \frac{e}{2\epsilon_0 \epsilon_r} (N_A x_p^2 + N_D x_n^2) \quad (4.2.7)$$

$$= \frac{e}{2\epsilon_0 \epsilon_r} x_p^2 \frac{N_A}{N_D} (N_A + N_D) \quad (4.2.8)$$

For the last step, the neutrality condition Equation 4.2.2 was used.

Typical values for V_{bi} in Silicon range from 0.4 to 0.8 V, depending on the doping concentrations.

From Equation 4.2.6, it is possible to calculate the depth of the depletion zone in the p-n junction:

$$x_p = \sqrt{\frac{e}{2\epsilon_0\epsilon_r} V_{bi} \frac{N_D}{N_A (N_D + N_A)}} \quad (4.2.9)$$

The calculation for x_n is equivalent, but N_A and N_D have to be swapped [12].

The ratio of the depletion depths is now just equal to the doping concentrations of the opposite side (Equation 4.2.10), therefore the depletion zone is larger in the less doped semiconductor.

$$\frac{x_p}{x_n} = \sqrt{\frac{N_D}{N_A (N_D + N_A)} \frac{N_D (N_D + N_A)}{N_A}} = \frac{N_D}{N_A} \quad (4.2.10)$$

For $N_D \gg N_A$, the contribution of x_n is negligible, the depletion depth subsequently calculates to:

$$d \approx x_p \approx \sqrt{\frac{2\epsilon_0\epsilon_r}{e} V_{bi} \frac{1}{N_A}} \quad (4.2.11)$$

4.3 p-n-Junction as Particle Detector

Now that the basics of semiconductors and diodes have been established, the important properties for particle detection can be discussed.

As mentioned in section 3, when a charged particle interacts with the material the deposited energy leads to ionization or excitation. If the particle passes through the depletion zone with the electric field it excites an electron into the conduction band, leaving behind a hole. It creates an *electron-hole pair*. This pair is instantly effected by the electric field in the depleted region, causing the electron and hole to move away from each other. Additionally, since there are very few free charge carriers, it is not probable for the electron (or hole) to recombine with another hole (or electron). The electron hole pair is accelerated in the electric field. This movement of the charge carrier induces a current signal on the readout electrode. The signal is then amplified by an amplifier and a comparator is used to differentiate between signal and noise. Further information about readout electronics is given in [18].

As the electric field is important to get a current signal, only the depleted region acts as the sensitive volume for particle detection.

In order to have a higher efficiency, the depleted region should be as large as possible. This can be done by applying an external bias voltage to the p-n-junction. The effects on

the depletion depth are dependent on the polarity and the size of the external voltage. If the applied bias voltage has a higher potential on the p-side than on the n-side, it is called *forward bias* ($V_{ext} > 0$). The voltage opposes the built in voltage and thus reduces the electron/hole drift. The diffusion current on the other hand is unaffected. Consequently, there are more electrons diffusing from the n-side to the p-side (for holes this is exactly opposite) and the depletion region reduces. For applied voltages over the built in voltage, a current in the sensor is visible.

If the applied voltage is negative ($V_{ext} < 0$), the external voltage increases the internal voltage, the effects reverse and the depletion zone increases in size. For the Equation 4.2.9 and Equation 4.2.11, V_{bi} has to be substituted by $V_{bi} - V_{ext}$.

Applying this to Equation 4.2.11, the voltage dependent depletion depth calculates to

$$d_p(V_{ext}) \approx \sqrt{\frac{2\epsilon_0\epsilon_r}{e} \frac{1}{N_A} (V_{bi} + V_{ext})} \approx 0.32 \sqrt{\frac{\rho}{\Omega cm} \frac{V_{ext}}{V}} \mu m \quad (4.3.1)$$

with $\rho \simeq (e\mu_h N_A)^{-1}$ being the substrate resistivity. The factor of 0.32 is only valid for silicon at 300 K.

4.4 Resistivity and Doping Concentration

Precise knowledge of the doping concentration allows a calculation of the depletion depth, a very important quantity for sensor operation, as shown above. In the production, a high precision for the doping concentration can not be guaranteed, therefore it needs to be measured. This can be done by measuring the resistivity using the 4-point probes method. In this method, four probes are placed in a straight line on the surface of the sensor. A current is applied through the outer two probes, while the inner two probes measure the voltage difference across a defined distance. Using $\rho \simeq (e\mu_h N_A)^{-1}$, the doping concentration is calculated from the resistivity. Although this is a simple method, it is not used in this thesis, as the probes can damage the sensor surface. Instead the doping concentration is determined indirectly via the capacitance measurements. This method is deduced from the symmetry of the junction. It is constructed by a charge free zone in between two oppositely charged zones, which resembles the form of a (plate)-capacitor. The depth W of the capacitor is equal to the depletion depth and thus dependent on the bias-voltage. Using the formula for the depletion (Equation 4.3.1), the capacity in Equation 5.1.5 computes to:

$$C(V) = \frac{\epsilon_0\epsilon_r A}{W(V)} = \frac{\epsilon_0\epsilon_r A}{\sqrt{\frac{2\epsilon_0\epsilon_r}{e} \frac{1}{N_A} V_{ext}}} \quad (4.4.1)$$

For a completely depleted capacitor the depletion depth equals the sensor depth and the capacitance remains constant with raising bias voltage. From a C-V-curve, the doping concentration can be calculated by rearranging this formula to:

$$d = \frac{\varepsilon_0 \varepsilon_r A}{C} = \sqrt{\frac{2\varepsilon_0 \varepsilon_r}{e} \frac{1}{N_A} V_{ext}} \Rightarrow N_A = \frac{2VC^2}{e\varepsilon_0 \varepsilon_r A^2} \quad (4.4.2)$$

Using $\rho \simeq (e\mu_h N_A)^{-1}$, the resistivity at room temperature can be calculated through

$$\rho = \left(\frac{\varepsilon_0 \varepsilon_r A}{0.32 \cdot C} \right)^2 \cdot \frac{1}{V} \quad (4.4.3)$$

From this formula, the $1/C^2$ dependence of the resistivity is visible. As the calculation of the resistivity is dependent of the mobility of the holes, Equation 4.4.3 is only valid at room temperature. For the calculation at different temperatures, the according mobility is needed.

The nominal value for the resistivity in the sensors in this thesis ranges from $200 \Omega \text{ cm}$ to $400 \Omega \text{ cm}$ at room temperature and the according doping ranges from $3.7 \times 10^{13} \text{ n}_{eq}/\text{cm}^2$ – $7.3 \times 10^{13} \text{ n}_{eq}/\text{cm}^2$. Measurements by the manufacturer resulted in a resistivity of $(369 \pm 21) \Omega \text{ cm}$. The sensors used in this thesis are homogenously doped.

Additionally, to the properties that can be calculated from the capacity, the capacity also determines the noise in the sensor. In order to have a high efficiency and precise time resolution in the sensor, the noise needs to be as low as possible. The two main sources for noise are current induced noise and capacitive noise from the readout and bulk material. Current induced noise is created by the intrinsic charge carrier creation which is temperature dependent (Equation 4.5.2). An increase in temperature leads to a higher current, which results in a higher charge induction on the readout electrode. For the capacity, the noise originates from scattering effects in the bulk. According to [19], the noise can be quantified using the equivalent noise charge (ENC), which allows an intuitive comparison of the noise to the signal. The ENC is given by

$$ENC^2 = a \cdot C^2 + b \cdot I_{leak} \quad (4.4.4)$$

Here, a and b are proportionality constants that depend on the sensor and readout.

4.5 IV-Curves

Even when the p-n-junction is under reverse bias, where ideally no current should flow, there appears to be a small leakage current I_L . This current originates from surface effects and bulk effects [12]. In the bulk, the creation of electron hole pairs are the main reason for the current. These are generated by thermal excitation or due to impurities or defects in the lattice, which introduce intermediate energy levels in the bandgap [20]. The leakage

current is proportional to the volume of the depletion, and since the depletion depth is proportional to the voltage (Equation 4.3.1) one finds:

$$I_L \propto A \cdot d \cdot \frac{n_i}{\tau_g} \propto A \cdot \sqrt{V_{bias}} \cdot \frac{n_i}{\tau_g} \quad (4.5.1)$$

Here, n_i is the intrinsic carrier concentration and τ_g is the charge carrier generation lifetime. This is a constant describing the lifetime of as a charge carrier before recombining. It is influenced by the thermal velocity of charge carriers and thus has a temperature dependence of $\tau_g \propto \frac{1}{\sqrt{T}}$, which together with Equation 4.1.11 for n_i results in

$$I_L \propto A \cdot d \cdot T^2 \exp\left(-\frac{E_G}{2kT}\right) \quad (4.5.2)$$

4.6 Radiation-effects

As mentioned in subsection 2.2, the sensors are exposed to high radiation levels, while the performance has to satisfy the requirements at all times. Therefore it is important to understand the effects of radiation on the sensor in order to guarantee successful operation. There are two kinds of radiation: Ionizing Energy Loss (IEL) and non-ionizing Energy Loss (NIEL).

Ionizing damage results from radiation with charged particles and photons. These ionize the material and create free electrons and holes, in a similar manner as mentioned in subsection 4.5. The IEL causes charge accumulations at the SiO₂ interface and can lead to bit flips in the readout electronics.

For the non-ionizing radiation, the damage affects mostly the bulk region. In contrast to the ionizing radiation, the particles responsible for the damage are hadrons, therefore particles with a high mass in respect to their charge. The NIEL is expressed in terms of the 1 MeV neutron equivalent fluence (n_{eq}/cm^2), which represents the fluence of 1 MeV neutrons that would cause the same displacement damage as the radiation under consideration. According to the NIEL-hypothesis [21], this equivalence allows for a consistent comparison of displacement damage caused by different particle types and energies. The equivalent fluence is calculated by scaling the actual particle fluence with the corresponding NIEL scaling factor.

In the material, these particles collide with the atoms, creating different kinds of defects: If an atom is knocked out of its original place, it leaves behind a *vacancy*. This vacancy acts as a trap for electrons or holes and therefore leads to a higher recombination rate.

The atom which is knocked out of its original lattice place ends up in between regular lattice spots. This so-called *interstitial* disturbs the silicon lattice. The effect is similar to a vacancy, as a higher recombination rate is created. Vacancies and interstitials together create a *Frenkel-pair*. These are the most common defects, further explanation can be

found in [22]. A schematic view of lattice defects can be seen in Figure 9.

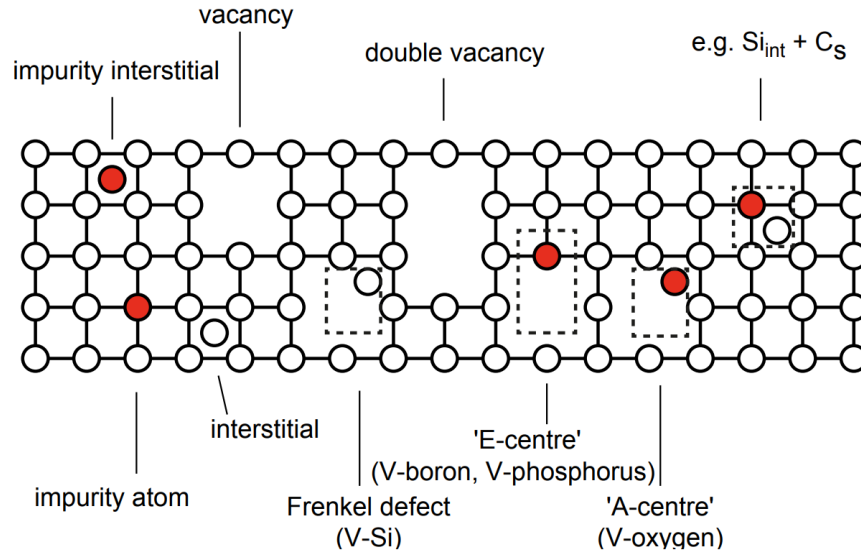


Figure 9: Different kinds of lattice defects in irradiated silicon. [12]

Both defects act as intermediary energy levels in the band gap (see Figure 10), making it possible for electrons to transition to the conduction band in steps. Thus less energy is needed and the charge carrier concentration is increased and there is a higher leakage current. On the other hand, the lifetime of these charge carriers is decreased through higher recombination rate from defects.

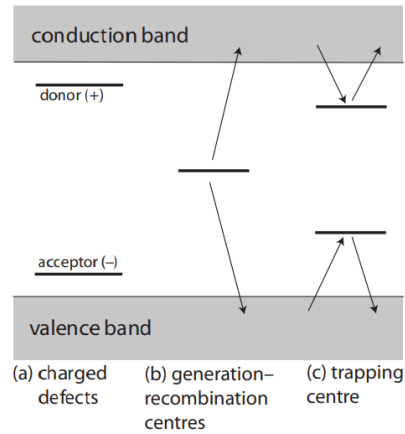


Figure 10: Location of intermediary energy levels in the bandgap, caused by substrate defects. [12]

The radiation does not only effect the silicon atoms, but also the impurity atoms introduced through doping. If a doping atom is knocked out of its lattice position, it loses its effect

on the doping concentration. Subsequently, non ionizing radiation decreases the doping concentration and results in a higher resistivity. For a high ohmic bulk (a bulk with low doping), the radiation effects are higher, as displaced impurity atoms have a higher relative effect.

The emergence of intermediary energy levels leads to a further complication for the calculation of the sensor properties. As mentioned in Equation 4.1.11, the intrinsic charge carrier concentration is proportional to the band gap. As the intermediary levels form, the value for the band gap decreases and the intrinsic charge carrier concentration increases. Furthermore, the temperature dependence increases with smaller E_G . The damage in the bulk can be mitigated by heating the sensor, in a process called annealing. By heating the sensor, the lattice vibrations increase and the interstitials can move back into the lattice. Higher movement for interstitials increases the recombination of vacancies and interstitials, thus decreasing the damage. Annealing the sensor too long at too high temperatures leads to reverse annealing, thus the emergence of further defects. In general, high annealing temperatures can break the sensor and therefore are not used. The effective doping concentration change after radiation and annealing can be calculated by [22]:

$$\begin{aligned} \Delta N_{eff}(t, \Phi, T) = & g_A \exp\left(\frac{-t}{\tau_A}\right) \Phi + N_{C,0} (1 - \exp(-c\Phi)) \\ & + g_C \Phi + g_Y \left(1 - \exp\left(\frac{-t}{\tau_Y}\right)\right) \end{aligned} \quad (4.6.1)$$

Here, t is the annealing time, T the annealing temperature and τ_i describes the carrier lifetime. g_A, g_C and g_Y are detector dependent constants. For these constants there is no reliable source for the sensors used in this thesis. The original formula is determined from n-type substrate, while modern sensors have p-type substrate. For a n-type high resistivity sensor, the effective doping after annealing at 60 °C is depicted in Figure 11.

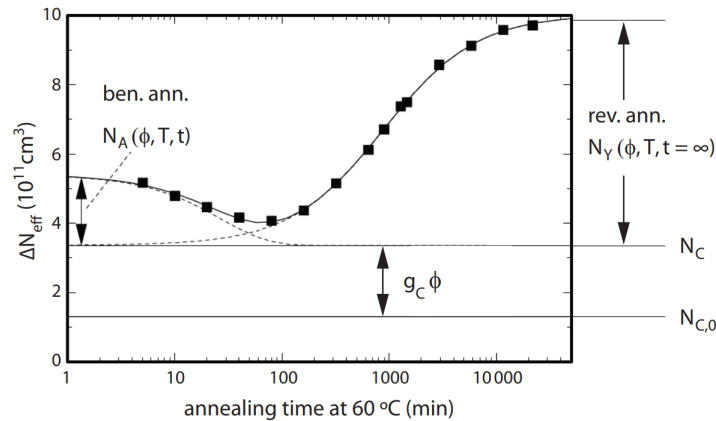


Figure 11: Effects of annealing on the doping concentration of a high ohmic n-type substrate[22]

A similar curve can be expected for the sensors in this thesis, but a quantified result is not currently known.

4.7 HV-MAPS

There are two kinds of pixel sensors commonly used: monolithic sensors and hybrid sensors. The difference between the two kinds of sensors lies in the construction of readout and detection region. Hybrid pixel sensors consist of two separate chips - a sensor chip for particle detection and a readout chip for signal processing. These are connected via bump bonding, a process that allows each chip to be individually optimized for its specific function, resulting in high performance. However, hybrid sensors typically have a higher power consumption and the bump bonding is a challenging and cost intensive process. In contrast, monolithic pixel sensors integrate both the detection and readout electronics in the same chip. This offers the advantage of lower power consumption and simpler manufacturing. Furthermore, the material budget in monolithic sensors is very low, which reduces the effect of multiple scattering. A schematic of both sensors types is shown in Figure 12.

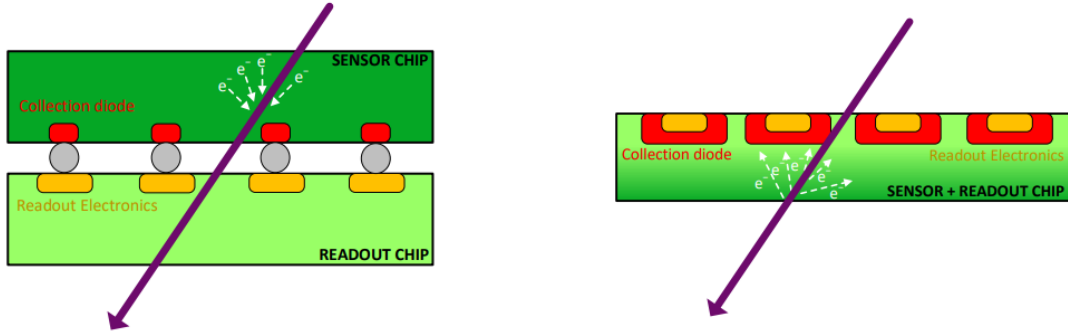


Figure 12: Schematic of Hybrid Pixel sensors (left) and monolithic pixel sensors (right) [23]

Due to the high costs of hybrid sensors, monolithic sensors, in particular **H**igh-**V**oltage **M**onolithic **A**ctive **P**ixel **S**ensors, are proposed to be used in LHCb.

HV-MAPS are manufactured using commercial high voltage CMOS technology. The substrate of the HV-MAPS is p-doped and each pixel has the readout electronics embedded within an n-well at the top. The application of a high reverse bias voltage - typically in the order of 100 V - creates a depleted region for the particle detection as mentioned in subsection 4.3. The periphery of the chip contains further readout and control logic, such as buffers and Digital to Analog Converters [24]. A schematic of an HV-MAPS with readout electronics is shown in Figure 13

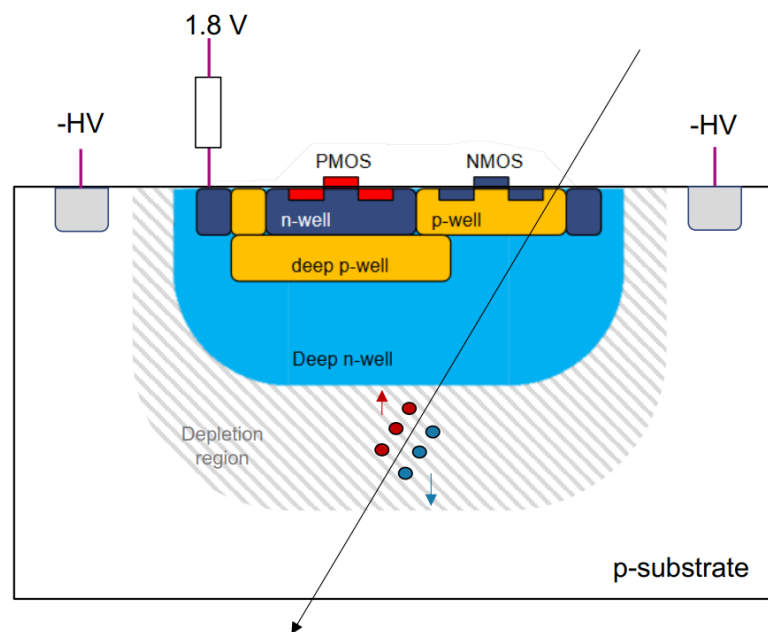


Figure 13: Working principle of an HV-MAPS [25].

5 RC-Circuits

The measurements in this thesis utilize the characteristics of electrical circuits, specifically on circuits consisting of capacitors and resistors. Therefore a short introduction to the functionality of capacitors is given, as well as an overview of AC behaviour of RC-Circuits.

5.1 Plate capacitor

Understanding the physics of the plate capacitor is essential, as the structure of the pixel sensor resembles a similar structure. This derivation of the formulas for plate capacitors follows [26].

A plate-capacitor consists of two parallel charged plates with charge Q , situated at a distance d . For the calculation, we first assume the area between the plates to be a vacuum. The electric field in the capacitor can be calculated using Gauss's law on a cylindrical surface vertical to the plates, with cross-section A [26]:

$$\oint_{\partial V} \vec{E} \cdot d\vec{A} \stackrel{\vec{E} \perp A}{=} E \cdot A = \frac{Q_{inside}}{\varepsilon_0} \quad (5.1.1)$$

Here, $\varepsilon_0 = 8.854 \times 10^{-12} \text{ F m}^{-1}$ [26] is the electric field constant.

Assuming a constant surface-charge density $\sigma = \frac{Q}{A}$, the electric field computes to:

$$E = \frac{\sigma}{\varepsilon_0} = \frac{Q}{\varepsilon_0 A} \quad (5.1.2)$$

Because of the constant surface density, the electric field has the same magnitude anywhere between the plates, it is *homogenous*. As the voltage between the two plates is defined as the line integral along the distance, for a homogenous field this simplifies to

$$U = E \cdot d = \frac{Q}{\varepsilon_0 A} \cdot d \quad (5.1.3)$$

Per definition, the capacitance is the ratio of charge Q to voltage U , therefore:

$$C_{vac} = \frac{Q}{U} = \frac{\varepsilon_0 A}{d} \quad (5.1.4)$$

If the volume in between the plates is filled with a dielectric material characterised by the relative permittivity ε_r , the actual capacitance is equal to the product of C_{vac} and ε_r . In the case of the detectors the material is silicon with $\varepsilon_{Si} = 11.7$ [16].

$$C = \frac{\varepsilon_0 \varepsilon_r A}{d} \quad (5.1.5)$$

5.2 Capacitor behaviour in an AC

The capacitance of a component is commonly measured based on its behaviour in an AC circuit in combination with a resistor.

In contrast to direct current *DC*, where voltage and current are constant over time, the current and voltage in the alternating current *AC* are following a sine curve. Both quantities can be described using the complex representation:

$$I(t) = I_0 e^{i(\omega t + \varphi)} \quad (5.2.1)$$

$$U(t) = U_0 e^{i\omega t} \quad (5.2.2)$$

Here, $\omega = 2\pi f$ denotes the angular frequency of the AC signal, and φ represents the phase shift between voltage and current.

The behaviour of a capacitor under AC can be described in a simple way:

First, the time dependent charge of the capacitor is given by the definition of capacitance (see Equation 5.1.4):

$$Q(t) = C \cdot U(t) = C \cdot U_0 e^{i\omega t} \quad (5.2.3)$$

Since the current is defined as the time derivative of the charge, the following expression is obtained:

$$I(t) = \frac{dQ(t)}{dt} = C \cdot U_0 \frac{d e^{i\omega t}}{dt} = C \cdot U_0 i\omega e^{i\omega t} \quad (5.2.4)$$

This equation shows the relation of current and voltage in a capacitor. The phase shift of 90° (or $\frac{\pi}{2}$ radians) for a capacitor becomes evident from the imaginary unit $i = e^{i\frac{\pi}{2}}$. This indicates that the current leads the voltage by a quarter period in a purely capacitive AC circuit.

Analogous to the resistance in DC, for AC the ratio of voltage and current is known as the impedance:

$$Z(t) = \frac{U(t)}{I(t)} \quad (5.2.5)$$

For the capacitor this results in

$$Z = \frac{U(t)}{I(t)} = \frac{U_0 e^{i\omega t}}{C \cdot U_0 i\omega e^{i\omega t}} = \frac{-i}{\omega C} \quad (5.2.6)$$

showing that the impedance is a complex quantity. The measurable quantities of the impedance are the absolute value $|Z|$ and the angle φ between the real and imaginary part, with $Z = |Z| \cdot e^{i\varphi}$ being the complex representation. This angle is the equivalent to

the phase shift of voltage and current. For an ideal capacitor, this leads to the same result as the calculation above:

$$\lim_{\operatorname{Re}(Z_C) \rightarrow 0^+} \arctan\left(\frac{\operatorname{Im}(Z_C)}{\operatorname{Re}(Z_C)}\right) = \arctan(-\infty) = -90^\circ \quad (5.2.7)$$

5.3 RC-Circuits

For a capacitor, the impedance is frequency dependent, the phase shift on the other hand is constant. However, if one has a circuit consisting of a capacitor and a resistor, the phase is also frequency dependent.

An ohmic resistor is not influenced by the alternating current:

$$|Z_R| = R \quad (5.3.1)$$

$$\varphi_R = \arctan\left(\frac{0}{R}\right) = 0 \quad (5.3.2)$$

In a serial connection, the total impedance is the sum of the individual impedances. So for a RC-Circuit the absolute value of the impedance and the phase result in:

$$|Z_{\text{series}}| = |Z_C + R| \quad (5.3.3)$$

$$\varphi_{\text{series}} = \arctan\left(\frac{-i}{\omega CR}\right) \quad (5.3.4)$$

As the impedance of the capacitor is inversely proportional to the frequency, for high frequencies the resistor dominates the impedance. The phase and absolute impedance curve for a serial connection of a capacitor of $C = 100 \text{ nF}$ and a resistor of $R = 1 \text{ k}\Omega$ can be seen in Figure 14. This type of diagram is called Bode plot. It depicts the frequency dependent behaviour of a circuit. For the serial connection, this shows that at low frequencies, the capacitor dominates the absolute impedance, while at high frequencies the resistor determines the system's response. This is also shown in the phase plot: at low frequencies, the phase-shift of -90° at low frequencies is characteristic for the capacitor and the 0° phase-shift at high frequencies is as expected for the resistor.

In a parallel connection, the total impedance is the inverse sum of the inverse partial impedances. This leads to:

$$|Z_{\text{parallel}}| = \left| \frac{Z_C \cdot R}{Z_C + R} \right| \quad (5.3.5)$$

$$\varphi_{para} = \arctan(\omega CR) \quad (5.3.6)$$

Again, the impedance of the capacitor is anti-proportional to the frequency, therefore at low frequencies the resistor dominates the impedance. As before, the phase and absolute impedance curve for parallel connection consisting of a capacitor of 100 nF and a resistor of $R = 1\text{ k}\Omega$ can be seen in Figure 14.

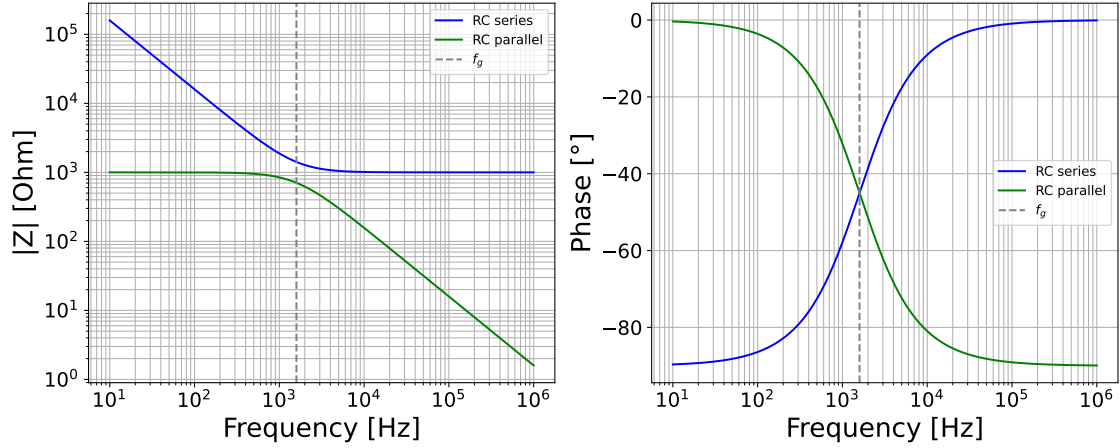


Figure 14: Bode plot for RC-Circuits ($C=100\text{nF}$ and $R=1\text{k}\Omega$)

For simplicity, the impedance in a parallel circuit will further be denoted as $Z_p = Z_1 || Z_2$. An important value for the RC-Circuit characterization is the cut-off frequency. This frequency is defined as the frequency where the phase shift reaches 45° , marking the inflection point. In serial RC-circuits, after this frequency the impedance is predominantly determined by the resistor. Conversely, for a parallel RC-circuit, it marks the point below which the impedance is mainly influenced by the resistor.

The cut-off frequency can be calculated using:

$$f_g = \frac{1}{2\pi RC} \quad (5.3.7)$$

6 Experimental Setup

6.1 The MightyPix1 Sensor

The sensor used in this thesis is the MightyPix1. It has been designed by Ivan Perić¹ et al. and functions as a prototype for the Mighty Tracker. The bulk is doped with boron (p-doped), with an n-well at the top in each pixel. Furthermore, each pixel has a CMOS amplifier and CMOS comparator embedded for the readout. The area of the sensor is $20\text{ mm} \times 5\text{ mm}$, with an active pixel area of $16\text{ mm} \times 4.785\text{ mm}$. This area consists of 320×29 pixels, each with a size of $50\text{ }\mu\text{m} \times 165\text{ }\mu\text{m}$. On the one side of the sensor, the digital parts are placed, such as Digital Analog Converters, the Clock, as well as bond pads that provide the electrical interface to the outside. The periphery where these parts lie acts as one large n-well. For this thesis, two different sensor thicknesses are used, $100\text{ }\mu\text{m}$ and $200\text{ }\mu\text{m}$, reached by thinning the material at the bottom. The n-well and readout electronics on top of the sensor have a thickness of $20\text{ }\mu\text{m}$, which needs to be subtracted from the substrate thickness. The dimensions of the n-well in each pixel are $135\text{ }\mu\text{m} \times 25.6\text{ }\mu\text{m}$, leaving a distance between n-well and pixel edge of $15\text{ }\mu\text{m}$ in one direction and $12.2\text{ }\mu\text{m}$ in the other. The nominal resistivity is $200\text{ }\Omega\text{ cm}$ to $400\text{ }\Omega\text{ cm}$. As can be seen in Figure 15, for measurement purposes the MightyPix1 is glued on to a copper plate of a customized PCB. Using the PCB, the sensor can be biased via the Pixel Guard Ring (PGR), which surrounds each pixel, or the Chip Guard Ring (CGR), which surrounds the entire pixel area. Each PCB contains a PT1000 thermometer, which can be used to measure the temperature at the sensor.

Property	value
Area	$20\text{ mm} \times 5\text{ mm}$
Pixel area	$16\text{ mm} \times 4.785\text{ mm}$
Pixel number	320×29
Pixel size	$50\text{ }\mu\text{m} \times 165\text{ }\mu\text{m}$
n-well	$25.6\text{ }\mu\text{m} \times 135\text{ }\mu\text{m}$
n-well margin	$12.2\text{ }\mu\text{m}, 15\text{ }\mu\text{m}$
$\rho_{nominal}$	$200\text{ }\Omega\text{ cm to }400\text{ }\Omega\text{ cm}$

Table 1: Table of the most important properties of the MightyPix1 [27].

¹Karlsruhe Institute of Technology (KIT)

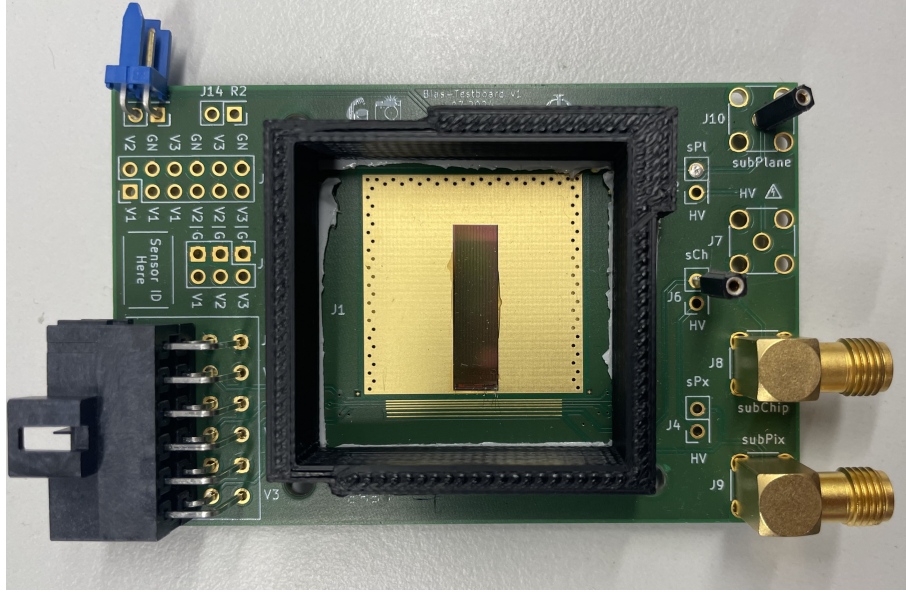


Figure 15: Close up Photo of the MightyPix1 glued onto the PCB used in this thesis.

6.2 Measurement Circuit

The capacity of the sensor is supposed to be measured using the frequency dependence of RC-circuits in AC. Therefore, the design for the measurement must satisfy three main requirements to be used in this thesis:

1. The sensor needs to be in connection to a resistor. On this circuit, an alternating current needs to be applicable in order to gain information of the capacity from the frequency dependency.
2. Possibility to apply a direct high-voltage to the sensor in order to deplete the sensor
3. Sensible dimensioning to achieve high sensitivity

The circuit used in this thesis consists of a capacitor connected in series with a parallel circuit containing the device under testing (DUT) and a resistor. The Direct Voltage is being applied to the parallel circuit using a Source Measure Unit, while the alternating current is applied to the outer circuit by an LCR-meter. Using this setup, the voltage across the sensor follows a sine curve shifted downward by the applied DC voltage, while the voltage at LCR-meter remains at the set limit. In addition to applying the alternating current, the LCR-Meter measures the resulting current and voltage waveforms. From these, the impedance and phase shift are calculated. A sketch of the circuit can be seen in Figure 16.

It is important to note that this is just one possible circuit design, but it satisfies the specified criteria.

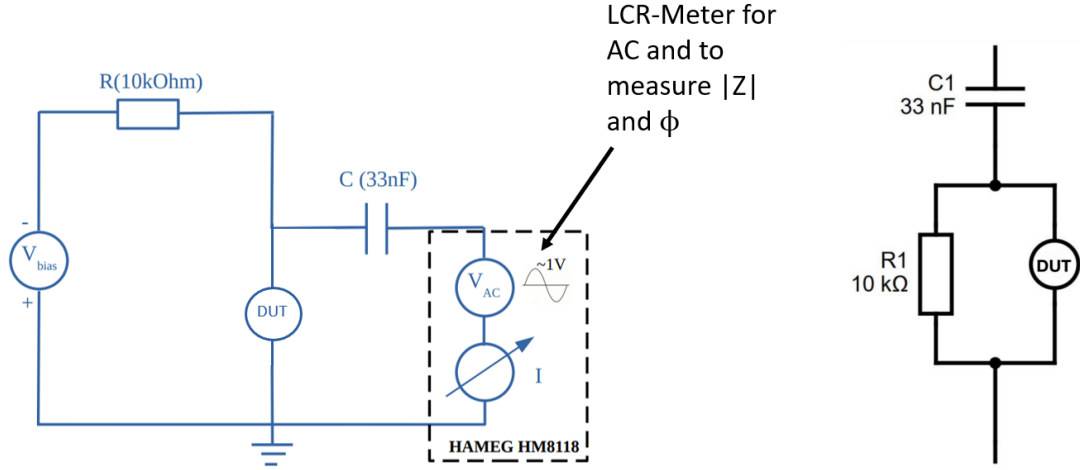


Figure 16: Measurement circuit used for the measurements in the thesis (a) and replacement circuit used for fitting (b).

For the third requirement, the dimensioning of the electric components is important. To ensure high sensitivity, the cut-off frequencies of both the parallel and serial circuit should lie in the measurable frequency range of 100 Hz to 200 kHz. By selecting cut-off frequencies of approximately 1.2 kHz and 16 kHz, the contributions of the two circuits can be clearly distinguished.

Starting with the parallel-circuit, the capacitance of the sensor is estimated for an assumed depletion depth of $70\text{ }\mu\text{m}$. This is in the common range of the depletion depth for the MightxPix1. For a resistivity of $370\text{ }\Omega\text{ cm}$ and an Area of $A=20\text{ mm} \times 5\text{ mm}$, the capacity computes to:

$$C_{70\text{ }\mu\text{m}} = \varepsilon_0 \varepsilon_r \frac{1\text{ cm}^2}{70\text{ }\mu\text{m}} = 148\text{ pF} \quad (6.2.1)$$

Converting Equation 5.3.7, a rough estimate for the resistor is computed, in order to get a cut-off frequency at 16 kHz.

$$R_{70\text{ }\mu\text{m}} = \frac{1}{2\pi f_g C_{70\text{ }\mu\text{m}}} = 67.5\text{ k}\Omega \quad (6.2.2)$$

The resistor used in the circuit is $10\text{ k}\Omega$. This leads to a higher cut-off frequency of the order of 50 kHz, but this is still in range.

For the serial connection of the capacitor with the parallel circuit, the formula for the cut-off frequency is a bit more complicated. To simplify the calculation, the parallel circuit is assumed as resistor alone, as the resistor is the main influence at this frequency. Using the resistance of $10\text{ k}\Omega$ and a cut-off frequency of 1.6 kHz, the capacitance calculates to

$$C = \frac{1}{2\pi f R} \approx 14\text{ pF} \quad (6.2.3)$$

The capacitor used in this setup is 33 nF, which shifts the cut-off frequency to lower frequencies, but still in the measurable range of the LCR-meter. The implementation of the circuit is shown in Figure 17.

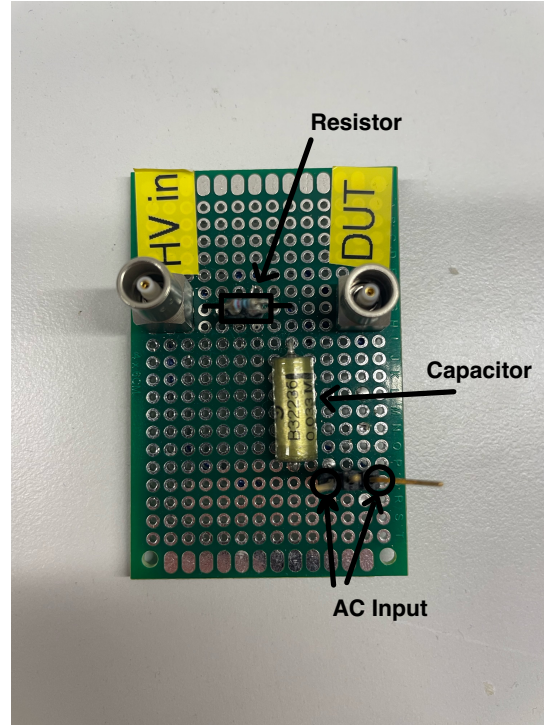


Figure 17: breadboard with the circuit used for the measurements

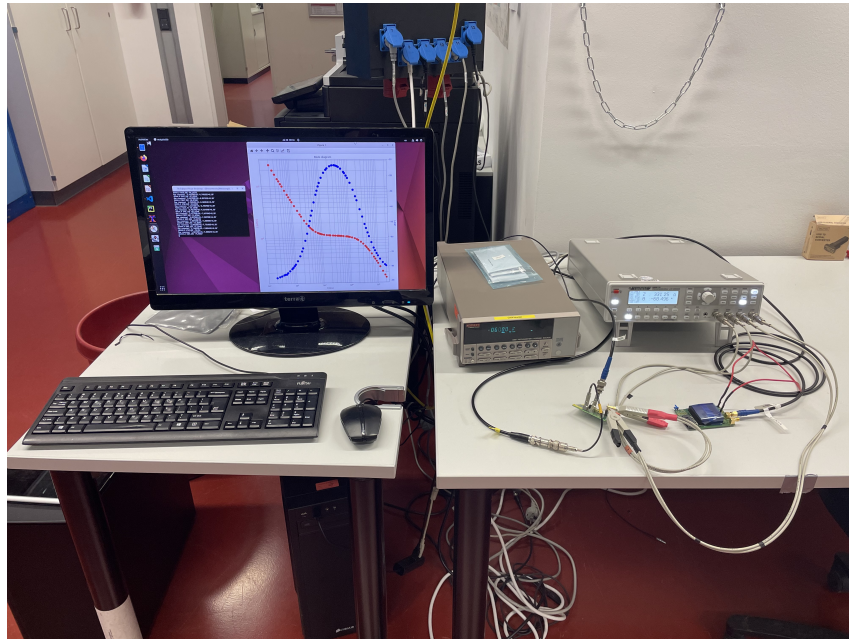


Figure 18: Photo of the measurement setup in the laboratory.

6.3 Set-up Validation

As this is the first time this setup is used, the functionality needs to be validated. Two main factors which are quantified by this are the effects of imperfect components and stray capacities. Furthermore, the simplification of the actual setup by the replacement circuit (see Figure 16 (b)) is analysed.

This is achieved using a simple capacitor as DUT (Device Under Test), where the expected results are already known and any offsets are directly observable. For this, a capacitor with a capacitance of 470 pF is soldered onto a SMA connector (see Figure 19). These SMA connectors, together with coaxial cables, are used to power the sensor to the setup, therefore minimizing further sources for offsets.



Figure 19: Capacitor soldered onto a SMA-connector for the validation measurements.

For the Capacitor, the $|Z|$ and φ - data is taken for the full frequency range from 100 Hz to 200 kHz. Under the assumption of the replacement circuit, the capacitance of the capacitor is determined by fitting the complex impedance to the measured data for both its magnitude and phase. The fitting formula is:

$$Z = Z_{33nF} + \frac{Z_R \cdot Z_C}{Z_R + Z_C} \quad (6.3.1)$$

with Z_C calculated using Equation 5.2.6 and $Z_R = R$. The fit is performed simultaneously on the magnitude $|Z|$ and the phase angle φ , providing a two dimensional evaluation. The data with the applied fit can be seen in Figure 20.

In the plot it is visible that the fit describes the data precisely, with only some minor variation in the residuals. The variations appear to be systematic and are attributed to the assumption made in the replacement circuit, which does not fully represent the actual

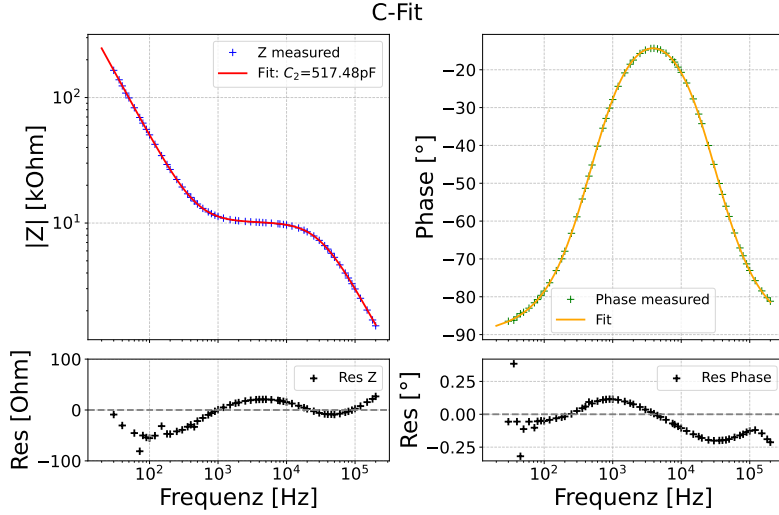


Figure 20: Two-dimensional capacitance-fit with residuals for a 470 pF Capacitor.

sensor. Nonetheless, the small deviations confirm that the replacement circuit provides an excellent approximation of the real circuit.

The second part which can be seen, is that the fit value is 517 pF and therefore a larger value than the expected 470 pF. In order to validate if this is a constant stray capacity, the same measurement is repeated for three further capacitors (for the fit-plots see subsection .2). This can be compared to the capacitance measured directly with the LCR-meter without breadboard or cable. The fit values, together with the LCR values and their difference can be seen in table Table 2.

$C_{LCR}[\text{pF}]$	$C_{fit} [\text{pF}]$	$\Delta C[\text{pF}]$
72	116	44
331	373	42
473	517	44
1117	1167	50

Table 2: Comparison of the capacitance values obtained from the fit using the complete setup with those measured directly by the LCR metre. ΔC is the difference between the two values.

One can observe a constant offset to larger capacities for the measurements with the breadboard and cable for all capacitors. This leads to the conclusion that a parasitic capacitance is present, which needs to be corrected for. The value for this capacitance is computed by plotting the fitted capacitance against the LCR-capacitance. The y-intercept of the linear fit through the data points gives the parasitic capacitance of 45 pF (see Figure 21). As the parasitic capacitance is highly dependent on the cable, it is determined for each cable and corrected for in the measurement.

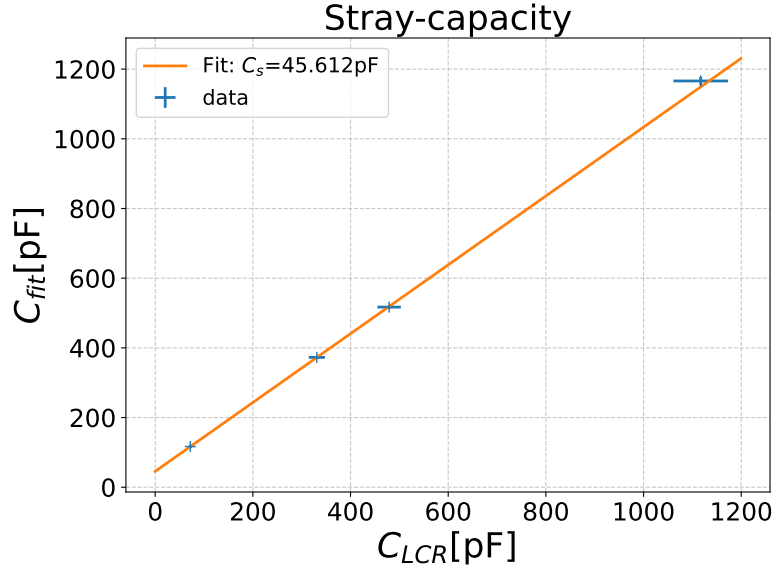


Figure 21: Plot of the capacitance values obtained from the fit using the complete setup against those measured directly by the LCR metre. The y-intercept of the linear fit gives the stray capacitance.

6.4 Measurement Procedure

Each measurement in this thesis works in the same way: the alternating current is applied to the circuit, with an amplitude of 1 V. This AC is applied during the entire measurement. Then the bias voltage is applied via the voltage supply. Unless stated otherwise, the starting bias-voltage is -2V. This leads to the voltage at the DUT following a sine curve determined by the AC, which is shifted by the bias-voltage (see Figure 22).

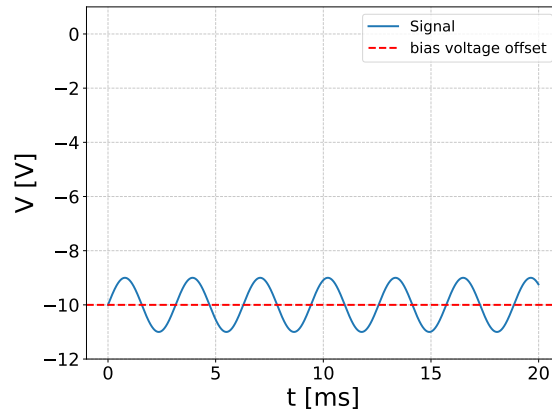


Figure 22: voltage over time at the DUT for an AC signal with $f = 300 \text{ Hz}$ and a bias voltage $V_{bias} = -10 \text{ V}$.

Keeping the voltage constant, the absolute impedance and phase-shift are measured for different frequencies using the LCR meter. After the frequency range is measured, the next voltage is applied. The voltage step size depends on the measuring range and on the characteristics of the curve. For measurements where details in the capacitance behaviour are important, a step size of 1 V or 2 V is used, while for measurements focusing only the general structure, a step size of 5 V is sufficient. In order to avoid being affected by charge-up effects, after each voltage increase there is a pause of 5 seconds before measuring, and for each frequency difference there is a pause of 1 seconds.

The LCR-meter quotes a relative uncertainty of the measurements of the impedance and phase-shift of below 0.1%. Due to the components used in the measurement setup having an uncertainty of 2%, the uncertainty of the measurement is assumed to be larger. In order to account for further deviations such as contact resistance, an uncertainty of 3% is chosen.

Though non conducting glue is used to fix the sensor onto to PCB, there is a voltage of approximately 60% of the bias voltage measurable on the backside contact of the sensor. In order to correct for this, the backside contact is shorted to the chip guard ring contact (Figure 23). In addition, for each sensor the IV-curve is measured under the same con-

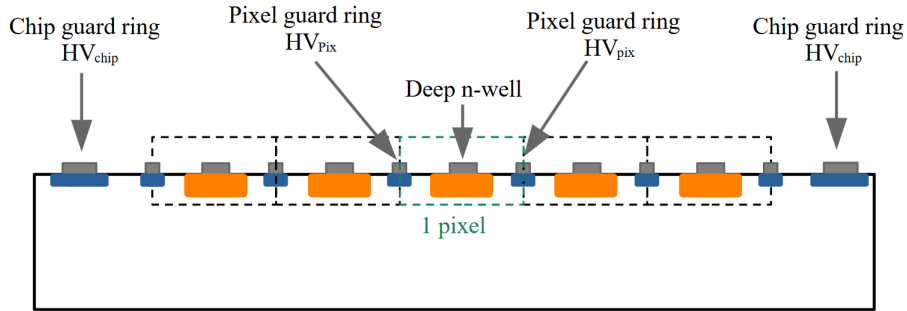


Figure 23: Side view of a simplified HV-MAPS showing the chip guard ring and pixel guard ring contacts. The backside contact is connected to the bottom of the sensor, which is not included in this sketch.

ditions as the capacitance measurement. This is done by applying a bias voltage using a source measure unit, which determines the current from the voltage drop across a precision internal shunt resistor.

6.5 Cooling Setup

As the temperature effects the current (Equation 4.5.2) and possibly also the capacitance, several measurements are performed in cooled conditions. For cooling, dry ice is used inside a laboratory freezer. During the measurements, the freezer is switched off, as its operation affects the measurement results. This influence is visible in the IV-curves shown

in [28]. By using dry ice, temperatures as low as -60°C are possible with minimal temperature fluctuations. However, varying the vertical position of the sensors in the freezer results in different temperatures. The temperature is measured using a PT1000 thermometer soldered onto the sensor PCB. Throughout the entire measurement series, all sensors remained inside the freezer, in order to operate the sensors in a thermal equilibrium.



Figure 24: Cooling Setup with dry ice used in this thesis.

7 Capacitance-Measurements

For all measurements the described capacitance measurement setup is used. Because of spatial constraints, the length of the cable connecting the DUT is adjusted where needed. As the stray capacitance is also dependent on the cable, for each measurement the according stray capacitance is subtracted.

The voltage range for the capacitance measurements is determined from the IV-measurement such that the maximum current does not exceed 50 μA , ensuring that the sensor is not damaged. Furthermore, both measurements can be compared to investigate bias voltage dependent effects.

As described in subsection 4.4, the CV-curve is described by $C \propto \frac{1}{\sqrt{V}}$ as higher voltage leads to higher depletion and therefore lower capacitance. When a sensor reaches full depletion, its capacitance remains constant with respect to the bias voltage.

7.1 Sensor Model

The sensor on which the model investigation is performed is the unirradiated 200 μm thick MightyPix1. To calculate the capacitance of the sensor from the measured impedance and phase shift, a model describing the sensor under test has to be chosen. Three different models will be investigated: a simple capacitor (C), a capacitor with a resistor in parallel (RpC) and a capacitor in series to a resistor (RsC). Further models with more fit-parameters such as two capacitors, with one being in series to a resistor will not be discussed, as these models do not improve the results and lead to unstable fits.

For the model comparison, an unirradiated sensor is to be used. The IV-curves for the two sensors in question are given in Figure 25. Both sensors follow a \sqrt{V} dependence at lower bias voltage, as the leakage current is proportional to the depleted volume, which increases with \sqrt{V} . For increasing voltages, the thinner sensor with a thickness of 100 μm shows an unexpected increase in current, presumably caused by complete depletion. However, the leakage current for the 200 μm thick sensor shows only a slight increase, caused by trap assisted tunnelling. The IV-curve shows the same behaviour as explained in [28]. Therefore, the 200 μm thick sensor is used for the sensor model comparison.

The three models are compared for a bias voltage of -60 V , -120 V and -180 V . This makes differences in the model accuracy at different depletion levels visible. For the fit, the same formula is used as for the validation:

$$Z = \frac{-i}{\omega 33\text{ nF}} + \frac{10\text{ k}\Omega \cdot Z_{\text{sensor}}}{10\text{ k}\Omega + Z_{\text{sensor}}} \quad (7.1.1)$$

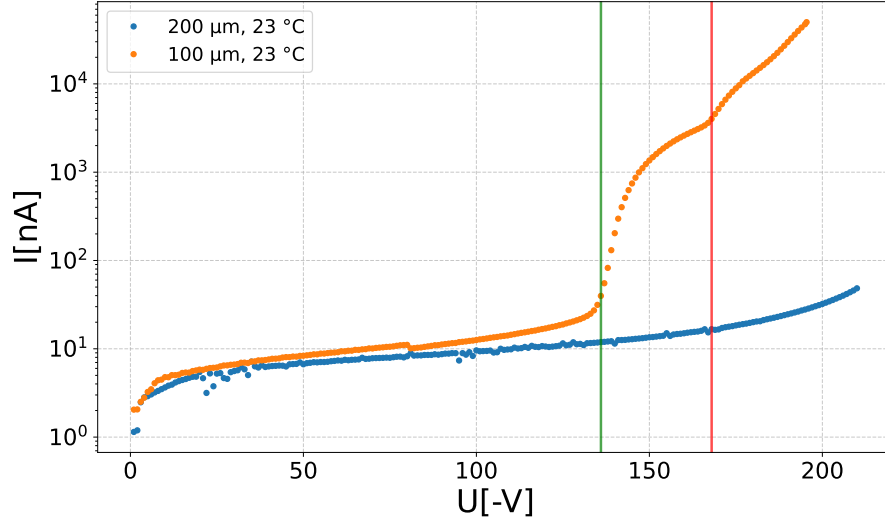


Figure 25: IV-curve of the unirradiated 200 μm and 200 μm thick sensor

with Z_{sensor} differing due to the used model:

$$Z_{\text{sensor},C} = \frac{-i}{\omega C} \quad (7.1.2)$$

$$Z_{\text{sensor},RsC} = Z_C + R \quad (7.1.3)$$

$$Z_{\text{sensor},RpC} = \frac{Z_C \cdot R}{Z_C + R} \quad (7.1.4)$$

The data for an applied voltage of -180 V along with the three fits is shown in Figure 26.

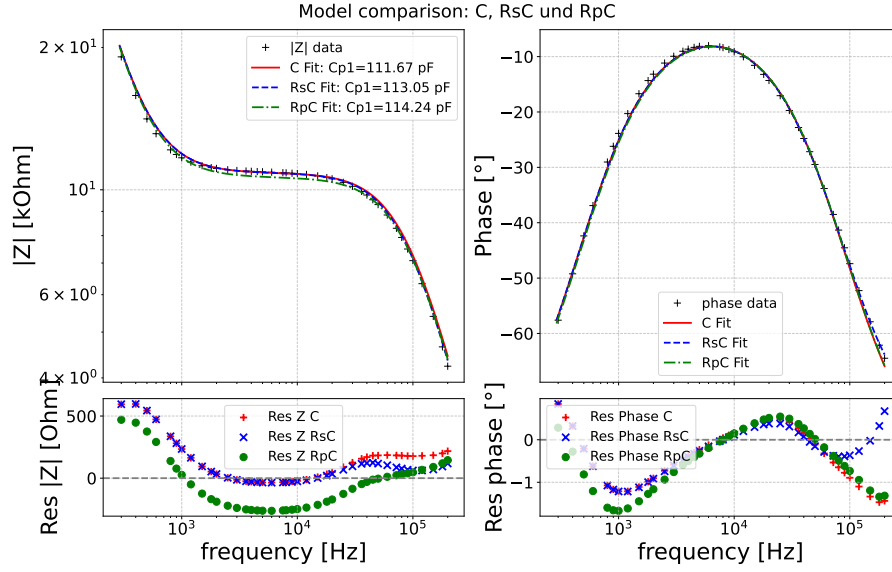


Figure 26: Comparison of the three fit-models with residuals for a bias voltage of -180 V. RsC refers to the serial model, RpC refers to the parallel model and C denotes the fit assuming a capacitor without resistor.

From this plot, it is visible that the three different fits all seem to describe the data in a reasonable manner and do not differ too strongly from each other. As for the capacitor, the residuals seem to depict a slight systematic deviation, confirming that there seems to be a small further influence on the data. However, the deviation is small and therefore neglected. For the comparison the χ_{red}^2 is calculated using

$$\chi_{red}^2 = \frac{\chi^2}{ndof} = \frac{\sum_{i=1}^n \left(\frac{|Z|_i^{theo} - |Z|_i^{exp}}{\sigma_{|Z|,i}} \right)^2}{ndof} + \frac{\sum_{i=1}^n \left(\frac{\varphi_i^{theo} - \varphi_i^{exp}}{\sigma_{\varphi,i}} \right)^2}{ndof} \quad (7.1.5)$$

The values for each fit are presented in Table 3.

	C	RsC	RpC
60V	$C = (189.6 \pm 2.1) \text{ pF}$ $\chi_{red}^2 = 1.6$	$C = (193.1 \pm 2.3) \text{ pF}$ $\chi_{red}^2 = 1.1$ $R = (549 \pm 11) \Omega$	$C = (192.5 \pm 2.2) \text{ pF}$ $\chi_{red}^2 = 2.3$ $R = (2.00 \pm 0.12) \text{ M}\Omega$
120V	$C = (135.7 \pm 1.6) \text{ pF}$ $\chi_{red}^2 = 1.4$	$C = (137.5 \pm 1.8) \text{ pF}$ $\chi_{red}^2 = 1.2$ $R = (536 \pm 16) \Omega$	$C = (138.1 \pm 1.6) \text{ pF}$ $\chi_{red}^2 = 2.2$ $R = (11.1 \pm 0.4) \text{ M}\Omega$
180V	$C = (111.9 \pm 1.4) \text{ pF}$ $\chi_{red}^2 = 1.3$	$C = (113.1 \pm 1.5) \text{ pF}$ $\chi_{red}^2 = 1.2$ $R = (518 \pm 23) \Omega$	$C = (114.2 \pm 1.4) \text{ pF}$ $\chi_{red}^2 = 2.2$ $R = (1.4 \pm 0.1) \text{ G}\Omega$

Table 3: Fitted Capacitance for the different models with the reduced χ^2 . RsC refers to the serial model, RpC refers to the parallel model and C denotes the fit assuming a capacitor without resistor.

The capacitance values do not differ too strongly and coincide in the error-ranges. The simple capacitor model results in the smallest capacitance value, while the series and parallel model are larger. Looking at the χ_{red}^2 , the serial model seems to describe the data the best, with the parallel mode giving the worst values. This can also be seen in the plot, where the parallel fit slightly deviates in the impedance across the full frequency range. Taking this, the fit-values at each voltage are plotted against the voltage (see Figure 27).

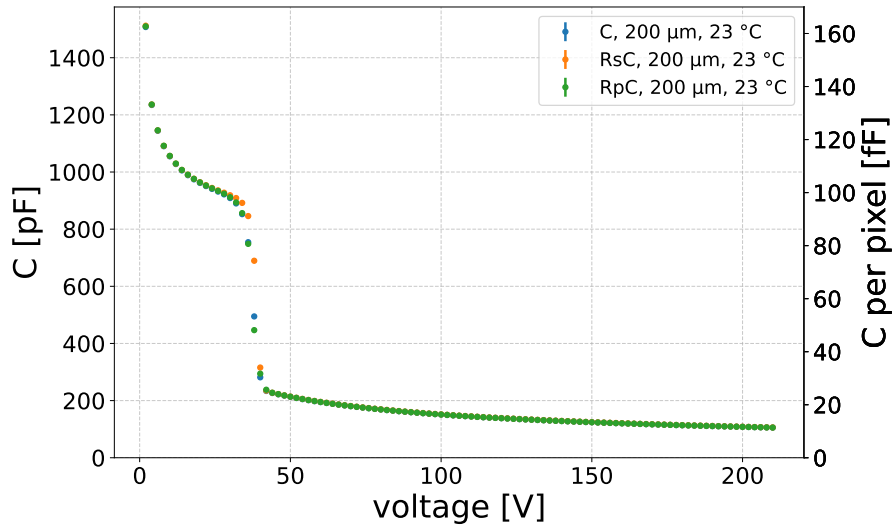


Figure 27: CV-curve for the 200 μm Sensor for all three models.

For voltages above -50 V the expected $1/\sqrt{V}$ behaviour can be observed. Below -50 V the measurement shows a behaviour which differs from the expectations. This effect is

discussed in section 9 and will be neglected for the following discussions.

Looking at the high bias voltages, the three models are barely different in the whole range and they each represent the expected behaviour.

In addition to the capacitance fit, the resistance fit value also gives further insights. For both models using a resistor, the according R-V-curve is shown in Figure 28.

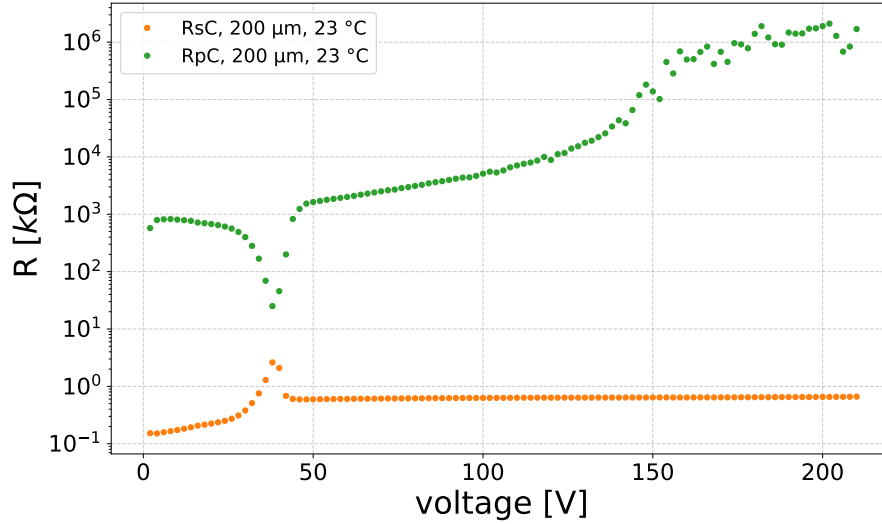


Figure 28: RV-curve for the 200 μm Sensor for the serial and parallel model.

Neglecting the area below -50 V , for the parallel model the resistance is very high, ranging from $1\text{ M}\Omega$ to $1\text{ G}\Omega$. This means, that the parallel resistors influence is low, as the impedances add inversely (see subsection 5.3). For the serial fit, the resistance computes to around $600\text{ }\Omega$. In a serial circuit, this resistance is not negligible. This explains why the serial fit provides the best agreement with the data.

Therefore, the serial model is chosen for the following investigations.

7.2 Sensor Thickness

Now that the sensor model has been established, the properties of the sensors can be analysed. In addition to the $200\text{ }\mu\text{m}$ thick sensor, a $100\text{ }\mu\text{m}$ thick sensor is investigated in order to observe the sensor behaviour under full depletion.

The IV-curve for the sensors is taken at room temperature and plotted in Figure 29.

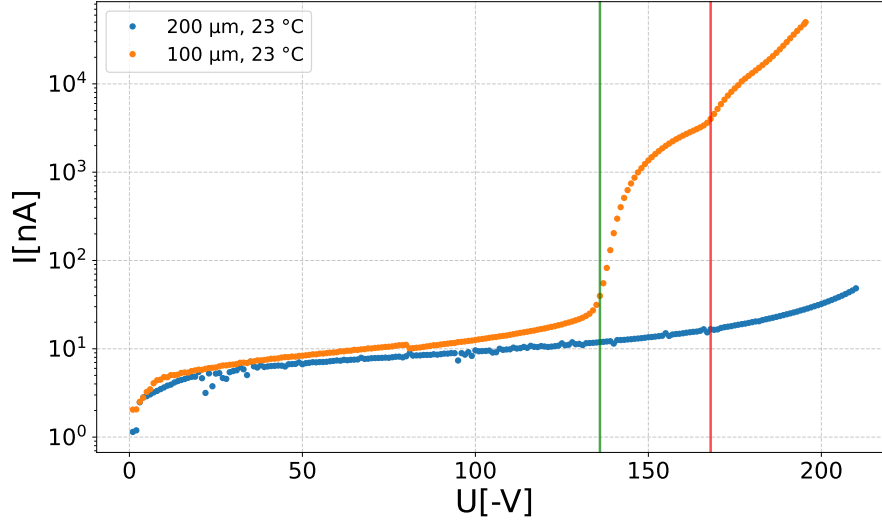


Figure 29: IV-measurements of the 100 μm and 200 μm thick sensor at room temperature. The green line indicates a bias voltage of -136 V and the red line of -168 V .

In Figure 29 it is visible, that the current is equivalent for both sensors up to a bias voltage of -136 V . At this bias voltage, the current of the 100 μm thick sensor shows a sharp increase, which is not visible for the 200 μm thick sensor. This sharp increase of current is caused by the depletion region reaching the damaged area at the backside of the sensor, as explained in subsection 6.1 (see also [29]). This increase continues up to bias voltages of -168 V , indicated by the red line in Figure 29. The current measurements for higher bias voltages depict an exponential increase. This indicates that the 100 μm sensor is completely depleted, as with increasing voltage the depleted volume remains constant but starts to heat up due to the current increase, resulting in the exponential growth according to Equation 4.5.2.

In the same manner as for the 200 μm sensor, the impedance and phase data is measured and the capacitance and resistivity is fitted using the serial model.

The CV-curve measurements for both sensors are plotted in Figure 30, together with the two lines where the IV-measurement shows noticeable features. One can observe the same behaviour for the two sensors as in the IV-measurement. The capacitance of the two sensors remains to be equal for voltages below -136 V , upon which the capacitance of the 100 μm sensor deviates to lower values. For bias voltages above -168 V the capacitance is constant. This confirms the assumption of complete depletion. One would expect that the capacitance of the thin sensor smooths out in the area of full depletion, as the depletion reaches the backside first in the centre and then spreads out to the edges. The thicker sensor undergoes further depletion with increasing bias voltage. However, the capacitance for the thinner sensor decreases in this area, which, like the leakage current, could also be caused by the damaged area on the backside.

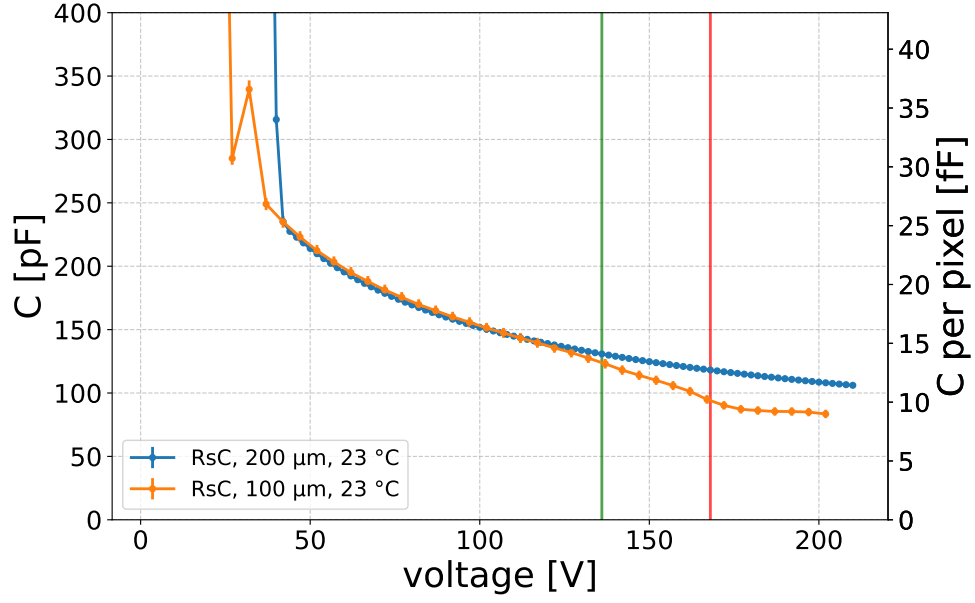


Figure 30: CV-curves for the 100 μm and 200 μm thick sensor at 23 $^{\circ}\text{C}$.

As mentioned in subsubsection 4.1.1, the CV-measurement can be used to calculate fundamental sensor properties. The depletion depth calculated using the assumption of having a parallel plate capacitor can be seen in Figure 31.

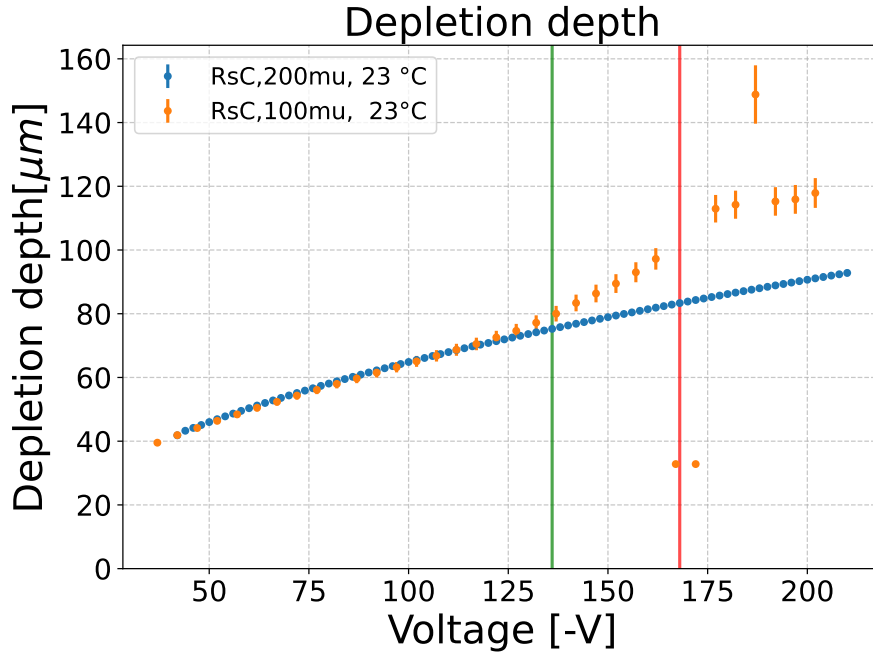


Figure 31: Calculated depletion of the 100 μm and 200 μm thick sensor.

For the calculation, the area of the capacitor is approximated as the area contained by the Chip Guard Ring including the digital part, i.e. 0.9504 cm^2 . This results in a depletion depth of $92 \mu\text{m}$ for the $200 \mu\text{m}$ sensor at -210 V . The actual area contributing to the capacitance is not precisely known. A rough estimate of the systematic uncertainty can be obtained by varying the assumed area. The minimal area is given by only using the pixel matrix size, excluding the readout electronics and periphery. This results in a depletion depth of $74 \mu\text{m}$, which seems implausible, as it would suggest that the $100 \mu\text{m}$ sensor is not yet fully depleted, contrary to indications from the IV-curve and the capacitance behaviour. On the other hand, the maximum area which can be assumed is given by the complete sensor area. The corresponding depletion depth is $97 \mu\text{m}$. Taking these two assumptions, a rough estimate of the systematic uncertainty on the depletion depth is about $\pm 5 \mu\text{m}$ to $\pm 10 \mu\text{m}$, depending on the bias voltage.

The depletion in Figure 31 shows the expected square-root behaviour for the $200 \mu\text{m}$ sensor, which is motivated by Equation 4.3.1. The $100 \mu\text{m}$ sensor shows the same depletion behaviour for bias voltages below -136 V . The unexpected capacitance and current behaviour at higher bias voltages correlates with the sensor being depleted down to the final $5 \mu\text{m}$ of its thickness. This region is affected by damage caused during the thinning process, which manifests as cracks in the material and irregularities in the lattice. These defects introduce intermediary energy levels in the bandgap, similar to the defects created by irradiation. For the sensor, this results in two main effects: an increase in leakage current as visible in Figure 29, and the creation of localized charge regions leading to electric field inhomogeneities. Since the electric field directly influences the capacitance, this could explain the observed decrease. As this influence is difficult to quantify, it is not possible to correct the capacitance values.

Equation 4.4.3 and Equation 4.4.2 can then be used to calculate the resistivity and doping concentration of the sensor.

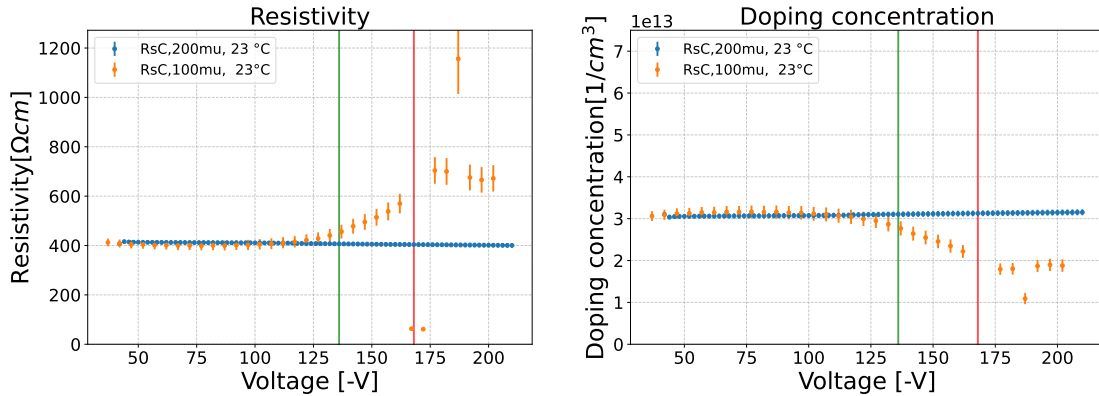


Figure 32: Resistivity and doping concentration for the $100 \mu\text{m}$ and $200 \mu\text{m}$ sensor calculated using the assumption of a plate capacitor

As expected, Figure 32 shows that for the 200 μm sensor the resistivity is measured to be constant over the voltage range, with only a slight decrease of around 3% visible from start to end. The resistivity is $\rho = (405 \pm 8) \Omega \text{ cm}$, which is in the expected range of 200 $\Omega \text{ cm}$ to 400 $\Omega \text{ cm}$ and agrees with the value of $(369 \pm 21) \Omega \text{ cm}$, measured by the manufacturer. As expected, the doping concentration is also constant (see Figure 32). With a value of $(3.21 \pm 0.06) \times 10^{13} \text{ cm}^{-3}$, the doping is in the expected range. Excluding the area above -136 V , the same doping concentration and resistivity are also found for the 100 μm thick sensor.

7.3 Measurements at lower temperatures

For the operation inside LHCb it is foreseen to cool the HV-MAP sensors, to ensure stable operating conditions and to reduce leakage currents. Therefore, it is important to understand how cooling affects the sensors depletion. For this, both the 100 μm and 200 μm sensor are investigated.

The sensors are cooled to -20°C using the cooling setup described in subsection 6.5. The IV characteristics of both sensors, measured at room temperature and under cooling, can be seen in Figure 33.

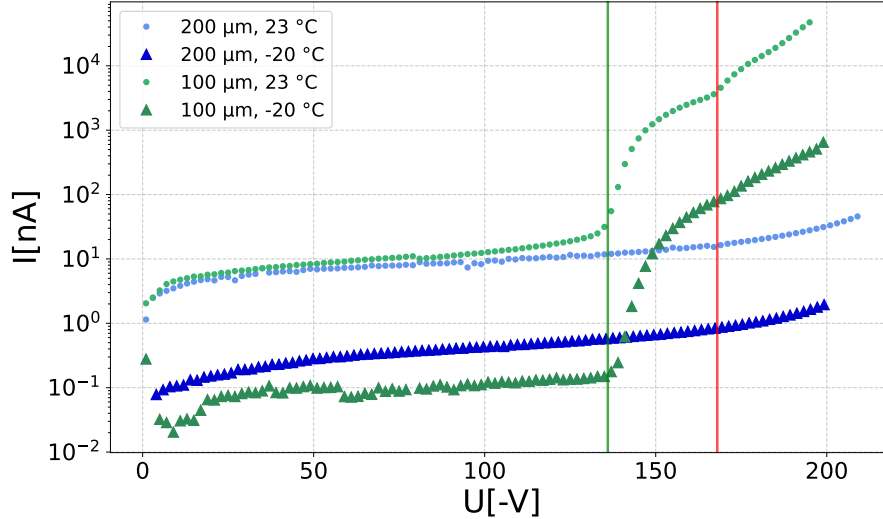


Figure 33: IV-measurements for the 100 μm and 200 μm sensors in cooled conditions and at room temperature as reference.

As expected from Equation 4.5.2, the leakage current is reduced in cooled conditions. Apart from this, no significant difference in the IV-characteristics for the two temperatures is observed.

Based on this observation, the impedance and phase shift is recorded for both sensors, and the capacitance and resistance is calculated using the serial model. As the doping concentration is not temperature dependent, the temperature is not expected to affect the capacitance.

A comparison of the CV characteristics of the 200 μm sensor at room temperature and under cooling is presented in Figure 34. As expected, both sensors show the same capacitance characteristic.

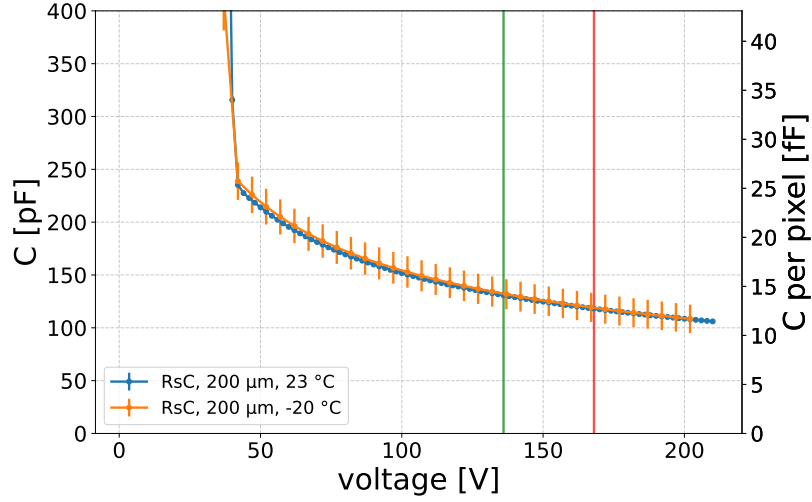


Figure 34: CV-measurements for the 200 μm sensors in cooled conditions and at room temperature as reference.

For the 100 μm the comparison of the CV-measurement is presented in Figure 35.

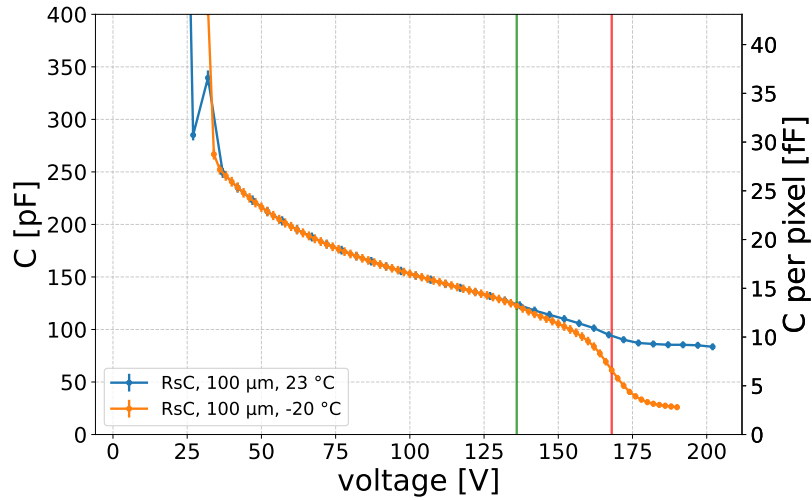


Figure 35: CV-measurements for the 100 μm sensors in cooled conditions and at room temperature as reference.

This plot shows that the capacitance is not affected by the temperature for bias voltages up to -136 V . The kink observed at room temperature at high bias voltages is also present in the cooled measurement. This kink is more pronounced at the lower temperature. Since the leakage current of the cooled $100\text{ }\mu\text{m}$ sensor is in a similar range as the current for the $200\text{ }\mu\text{m}$ sensor at room temperature, the kink can not be attributed to the high current alone. These measurements suggest that the damage introduced by the thinning process leads to further effects introducing a temperature-dependent behaviour.

8 Irradiated sensors

Previous measurements on irradiated sensors indicate that the irradiation alters the effective doping concentration of the sensor and subsequently affects the depletion depth [30]. The aim of the following measurements is to quantify the impact of neutron irradiation on the depletion characteristic of the sensor. For this purpose, sensors irradiated at the TRIGA Mark II reactor in Mainz [31] with neutrons fluences of $1 \times 10^{13} \text{ n}_{\text{eq}}/\text{cm}^2$, $5 \times 10^{13} \text{ n}_{\text{eq}}/\text{cm}^2$, $1 \times 10^{14} \text{ n}_{\text{eq}}/\text{cm}^2$ and $4 \times 10^{14} \text{ n}_{\text{eq}}/\text{cm}^2$ are investigated. All the irradiated sensors have a thickness of $200 \mu\text{m}$. Since irradiation is expected to lead to higher leakage currents, potentially interfering with the capacitance measurement, the sensors are measured at three different temperatures: at room temperature, -20°C and -50°C , in order to study the temperature dependence. The cold temperature measurements are performed by the cooling setup according to subsection 6.5.

As mentioned in subsection 4.6, for irradiated sensors the current per volume is higher than for unirradiated sensors and the current is proportional to the temperature (Equation 4.1.11). These effects are confirmed by the IV curve of the $1 \times 10^{13} \text{ n}_{\text{eq}}/\text{cm}^2$ and $5 \times 10^{13} \text{ n}_{\text{eq}}/\text{cm}^2$ irradiated sensors (see Figure 36). The current measurements for the higher irradiated sensor are each higher than the current on the lower irradiated sensor. Furthermore, the current at room temperature is significantly higher than in the measurement at -20°C . None of the leakage current measurements show visible effects such as backside touching.

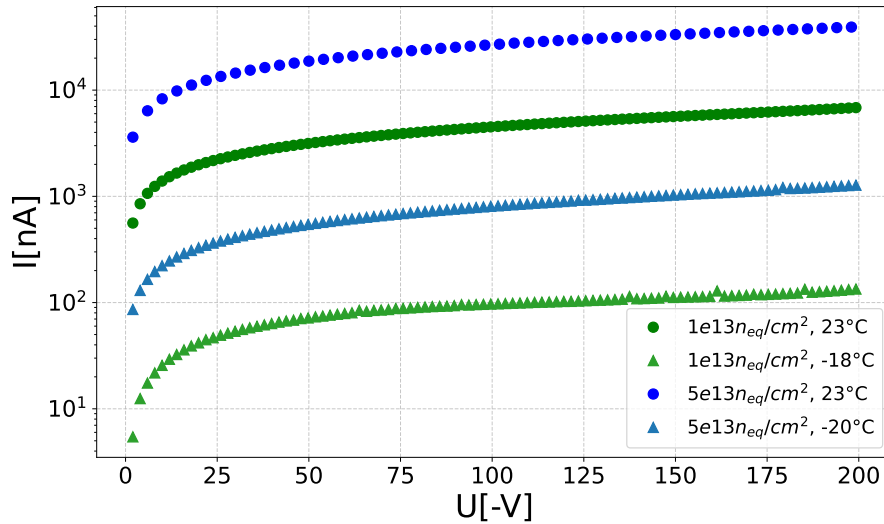


Figure 36: IV-measurements for the $1 \times 10^{13} \text{ n}_{\text{eq}}/\text{cm}^2$ (in green) and $5 \times 10^{13} \text{ n}_{\text{eq}}/\text{cm}^2$ (in blue) irradiated sensors at room temperature and at approximately -20°C .

For each capacitance measurement, the same procedure as for the unirradiated sensors is

used. The fit model continues to be the serial fit (a comparison of the different models for irradiated sensors is in subsection .3).

The CV-curves for the $5 \times 10^{13} \text{ n}_{\text{eq}}/\text{cm}^2$ irradiated sensor can be seen in Figure 37.

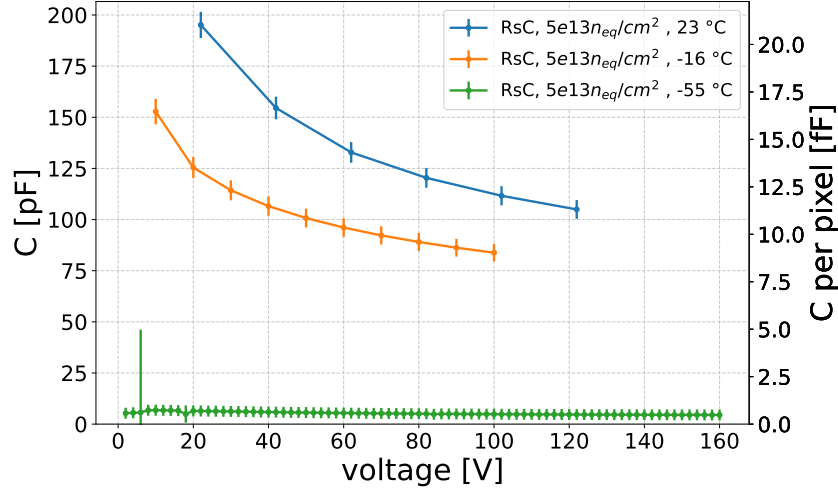


Figure 37: CV-curves for the $5 \times 10^{13} \text{ n}_{\text{eq}}/\text{cm}^2$ irradiated sensor at three different temperatures

Here, the effect of the temperature is obvious. The room temperature measurement seems to depict the expected \sqrt{V} behaviour still in a good manner. For the measurement at -20°C , the capacitance is shifted towards lower capacities, but a general $1/\sqrt{V}$ behaviour is still visible. This is not the case for the lowest temperature measurement, where the capacitance seems to be roughly constant with a value of $C = 5 \text{ pF}$. This capacitance behaviour is not physically sensible, especially as the capacitance value is lower than for a fully depleted sensor, which is $C_{\text{fulldepletion}} = 54.6 \text{ pF}$.

The effects of temperature appear to be more pronounced with higher irradiation, As can be seen for the capacitance of the $1 \times 10^{14} \text{ n}_{\text{eq}}/\text{cm}^2$ irradiated sensor depicted in Figure 38.

Again, the measurement at room temperature depicts a behaviour similar to the $1/\sqrt{V}$ shape. The capacitance for the measurement at -20°C still shows a decrease for low bias voltage, but is constant for bias voltages over -20 V . As for the $5 \times 10^{13} \text{ n}_{\text{eq}}/\text{cm}^2$ irradiated sensor, the constant value is too low to be caused by the depletion. The capacitance for the coldest measurement is also constant, and therefore not sensible for further analysis. Previous studies, such as Croitoru et. al. (1997) [32] show a similar constant capacitance behaviour at low temperatures. Below a certain critical temperature T_C , the measured capacitance becomes nearly independent of the applied bias voltage, and T_C increases with irradiation fluence. This effect is explained by the trapping of charge carriers in defect-induced energy levels“ Due to the low thermal energy, trapped carriers cannot be released. The electric field is no longer able to change with the alternating current and the measured capacitance depends only on the number of free charge carriers. Higher levels

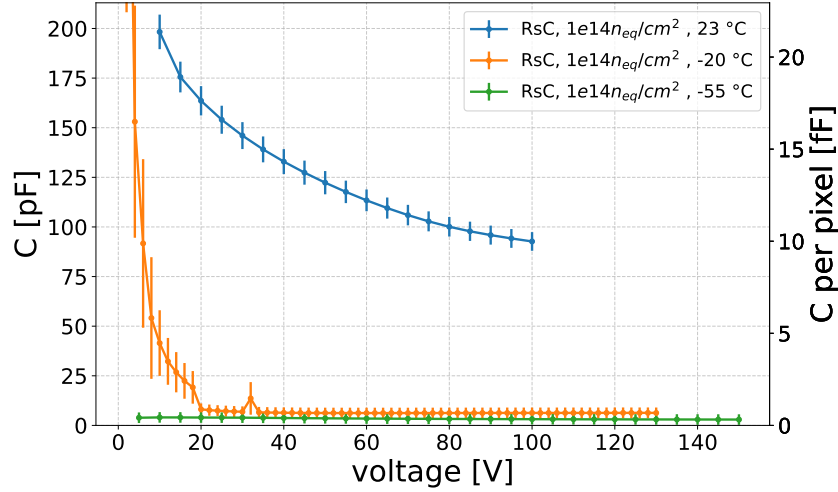


Figure 38: CV-curves for the $1 \times 10^{14} \text{ n}_{\text{eq}}/\text{cm}^2$ irradiated sensor at three different temperatures

of irradiation damage lead to more energy levels and thus a more pronounced electron trapping. It is important to note, however, that this study has been performed on n-type silicon with a higher resistivity of the order of $4 \text{ k}\Omega \text{ cm}$ to $6 \text{ k}\Omega \text{ cm}$, which differs from the sensors used in this work.

From the plots, the measurements at room temperature seem to be sensible for all irradiated sensors. For comparison, all CV measurements performed on $200 \mu\text{m}$ thick sensors at room temperature are depicted in Figure 39.

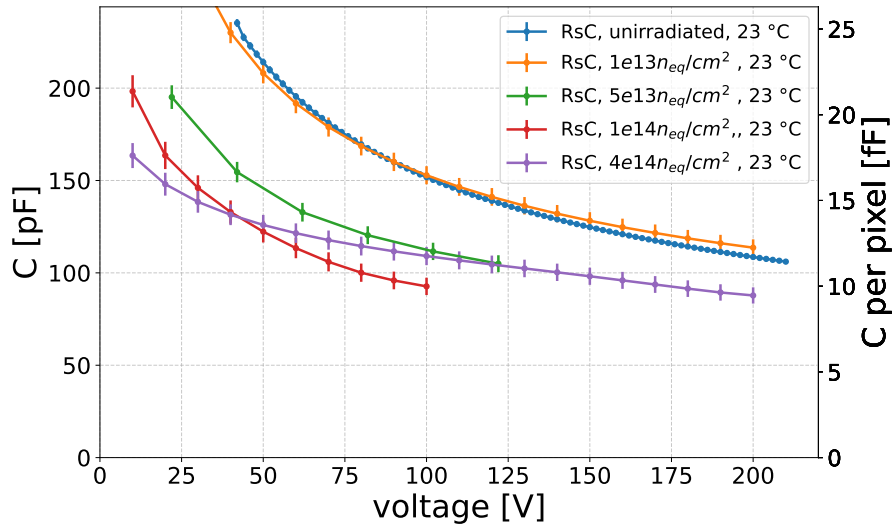


Figure 39: CV-measurements for all irradiates sensors at room temperature. For a better comparison, the capacitance for the unirradiated sensor is also shown.

There are several effects visible in Figure 39. The irradiation of the sensors leads to lower

capacities at equal bias voltages. This effect is more pronounced the higher the irradiation, with the $1 \times 10^{13} \text{ n}_{\text{eq}}/\text{cm}^2$ irradiated sensor showing only a small shift compatible with the uncertainties.

Furthermore, in the CV-measurement for the sensor irradiated with $4 \times 10^{14} \text{ n}_{\text{eq}}/\text{cm}^2$, the capacitance curve intersects with those from lower irradiated sensors. Based on the observed trends, further intersections are expected at higher bias voltages. This is not expected under the assumption of constant doping. A possible explanation is the presence of high leakage currents at increased bias voltages, which can influence the capacitance measurement by introducing an additional conductive path in parallel to the depletion capacitance. This leads to a phase shift in the measured impedance and can result in an apparent change in the extracted capacitance, particularly at high voltages where leakage is more pronounced.

For the measurements at room temperature, the depletion depths are still in a sensible range (see Figure 40).

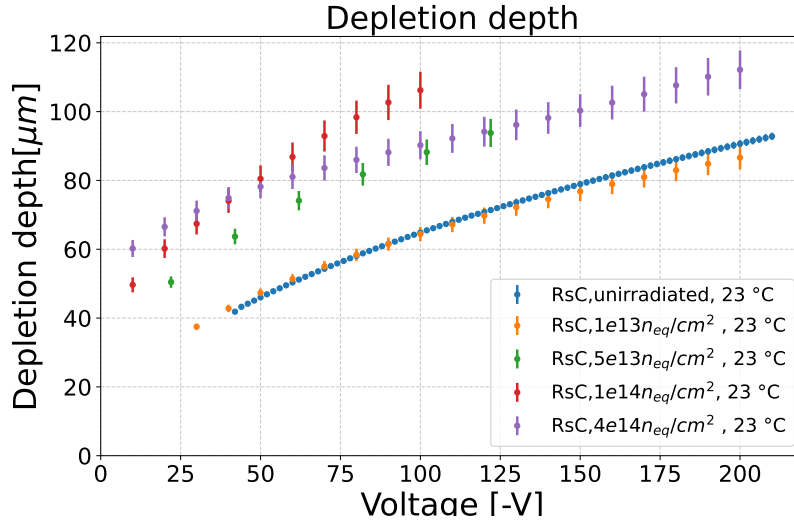


Figure 40: Calculated depletion depth for all irradiates sensors at room temperature.

However, plotting the doping concentration calculated from the capacitance indicates a non-constant doping concentration (see Figure 41). This shows, that the measurements at room temperature are already affected too strongly by further effects. For the cooled measurements, one observes that the capacitance is not sensible, thus a further analysis calculating the depletion depth or doping is not performed.

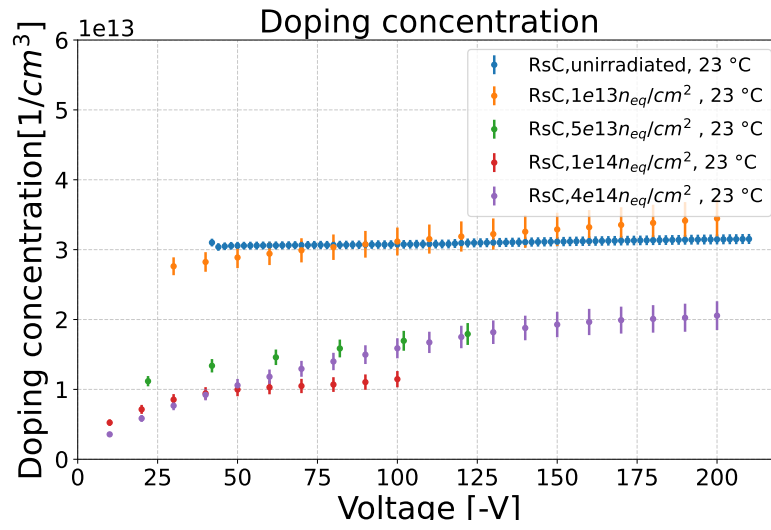


Figure 41: Calculated doping concentration for all irradiates sensors at room temperature.

9 Capacitance behaviour at low bias voltage

In the region of bias voltages below approximately -40 V, the measured capacitance shows a constant offset from the expected capacitance behaviour (see Figure 27). This deviation indicates the presence of an additional physical effect not accounted for in the applied model and is therefore investigated.

There are three CV-curves which show this unexpected behaviour: both unirradiated sensors and the $1 \times 10^{13} \text{ n}_{\text{eq}}/\text{cm}^2$ irradiated sensor. In the higher irradiated sensors, this is not observed. Plotting these measurements (see Figure 42) shows that the end of the offset for the different sensors ranges from 25 V to 40 V.

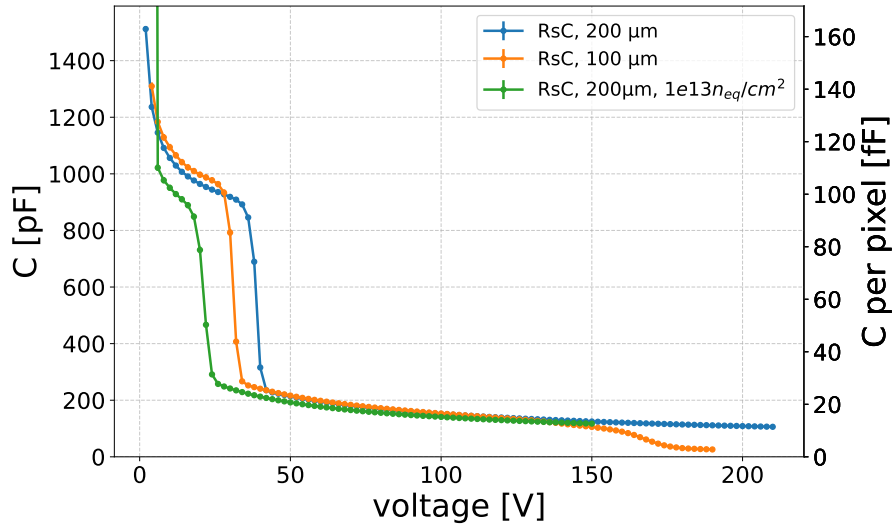


Figure 42: CV-curves for different sensors which all show an offset at low voltage.

The offset for the $200 \mu\text{m}$ thick sensor is visible for biases below -40 V, while for the thinner sensor it is visible for biases below -35 V. For the irradiated $200 \mu\text{m}$ thick sensor, the offset is at a significantly lower voltage of -25 V. If the observed offset arises from a geometric effect, it is important to investigate the corresponding depletion depth. The depletion for the three measurements is plotted in Figure 43.

It can be seen that the jump occurs at a depletion depth of approximately $40 \mu\text{m}$ to $43 \mu\text{m}$, with small variations between the sensors. This indicates that the change in capacitance is caused by a geometric effect. The small variations in the depletion can result from small differences in the doping concentration between the sensors and measurement uncertainties.

For the low bias voltage area there are several aspects interfering with the measurement,

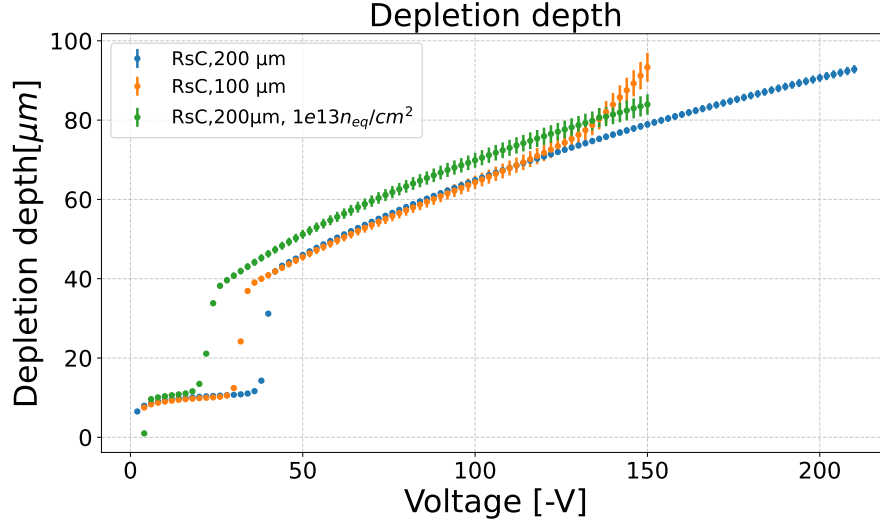


Figure 43: depletion depth for different sensors which all show an offset at low voltage.

which could be the cause for this offset. Firstly, the readout electronics are directly connected to the sensor nodes and can therefore introduce additional parasitic capacitances, for example through the input transistors of the preamplifiers, bond pads, and interconnects. From the perspective of the capacitance measurement, these contributions appear in parallel to the intrinsic sensor capacitance, leading to an overestimation of the latter for low bias voltages. Furthermore, at a low bias voltage, the approximation of the depletion region as a parallel plate capacitor is not valid. Instead the depletion spreads radially outward from the n-well, resulting in a non-uniform depletion depth along the z-direction. In particular, the depletion is larger at the centre of each pixel than at its edges. This spatial distribution is illustrated by the TCAD (Technology Computer-Aided Design [33]) simulation in Figure 44. TCAD refers to a class of simulation tools used to model the physical behaviour of semiconductor devices. The simulations are based on the Finite Element Method (FEM), which numerically solves the underlying physical equations in order to calculate properties such as the electric field or charge carrier concentration. In Figure 44, the simulation of the biasing of two adjacent pixels is shown, where the depleted region corresponds to the area in between the two white lines. Here, the low depletion in between the pixels is visible in the range of

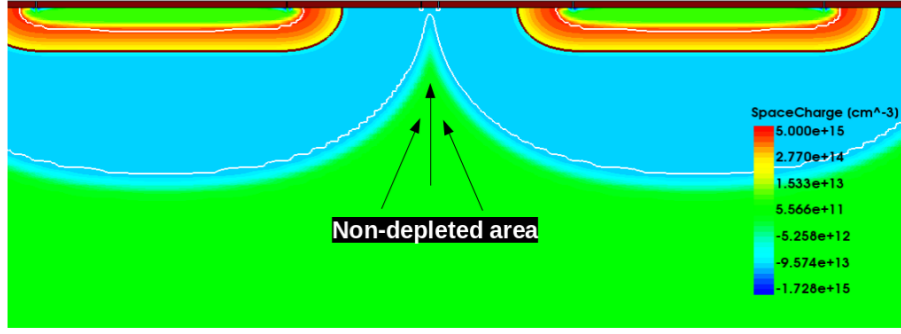


Figure 44: Side view TCAD simulation of the depletion in an HV-MAPS at low bias voltage. The depletion is depicted by the white lines. The space charge values do not correspond to the MightyPix1. [34]

Another possible effect is the lateral depletion of the pixel. The n-well has a distance of $12.2\mu\text{m}$ to one pixel edge and $15\mu\text{m}$ to the other. Applying a voltage, this margin is depleted at a bias of -3 V to -4 V , therefore it is unlikely that this is the reason for the offset.

As an additional hypothesis, the observed offset in the CV measurements could be related to an effect similar to one known from silicon drift detectors. Such a detector consists of two p-wells (depicted in green in Figure 45) embedded in an n-type substrate. By applying a voltage difference to the p-wells, depletion zones form around each well and expand until they get in contact. In the CV-measurement of the silicon drift detector, this contact is shown as a sharp drop in capacitance. The corresponding CV-measurement is shown in Figure 46, where the x-axis represents the bias voltage difference of the two p-wells.

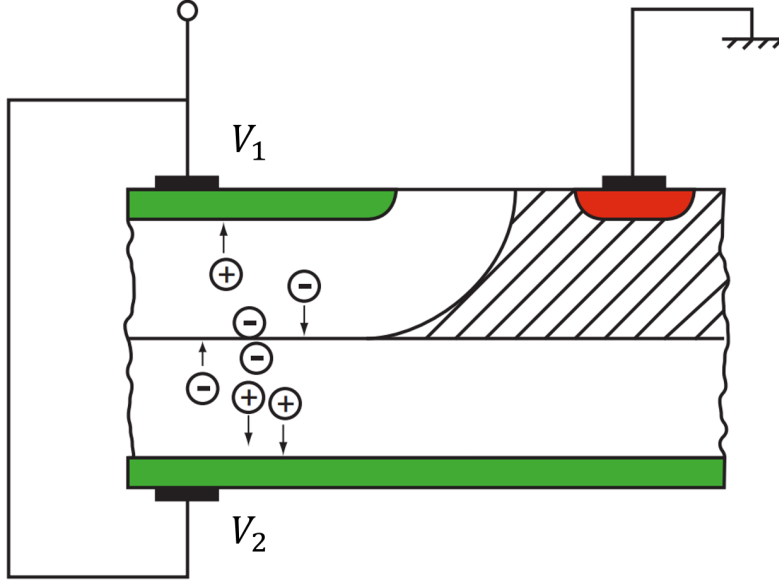


Figure 45: Schematic of a silicon drift detector. [12]

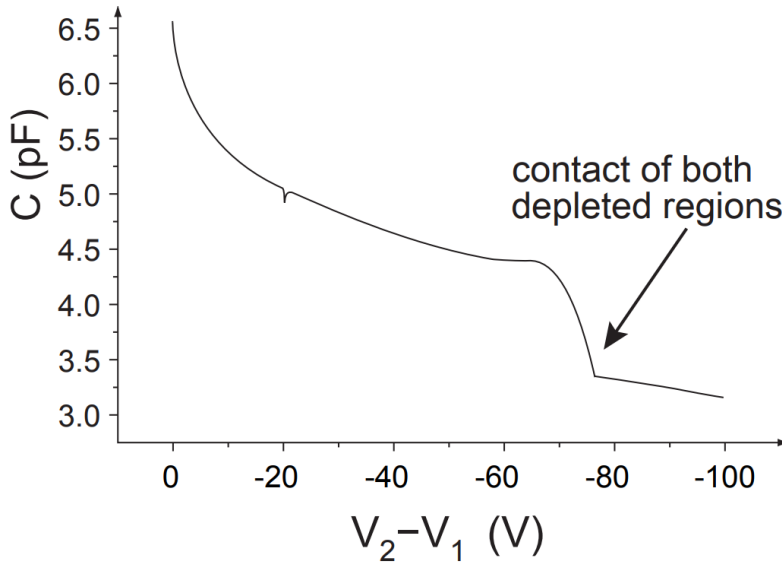


Figure 46: CV-curve of a silicon drift detector. [12]

In the MightyPix, such a contact can be found between the Chip guard ring and the isolation well (see Figure 47).

This spatial dependence of the offset would also explain the appearance at different bias voltages, as the depletion depth differs for the irradiated sensors.

In general, all the proposed hypotheses affect the measurement at low bias-voltages. Given the abrupt nature of the offset, it is unlikely that the readout electronics are responsible, as such an effect would be expected to gradually decrease with increasing bias voltage.

The sharp decline in capacitance at this voltages is best explained by the contact of the depletion zones. To confirm this hypothesis, measurements of sensors with different chip geometries are required. More precise measurements in the range between -5 V to 0 V would also be interesting to determine whether this effect is visible for depletions between Pixels. Additionally, more dedicated simulations of the depletion zones are needed.

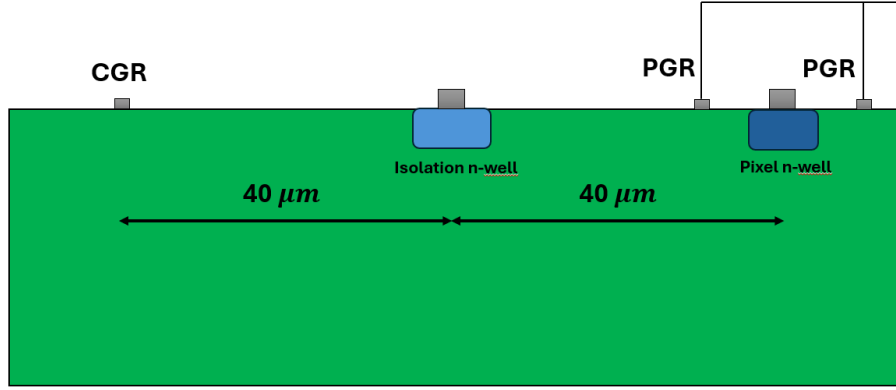


Figure 47: Schematic side-view of the MightyPix1 with the characteristic distance of $40\text{ }\mu\text{m}$ from the isolation n-well to the CGR and the edge pixel.

10 Conclusion and Outlook

10.1 Conclusion

In this thesis, a method for systematic capacitance measurements of HV-MAPS using impedance and phase-shift analysis of RC circuits is developed and tested. The method achieves accurate measurements while maintaining the full sensor functionality making it relevant for quality control applications.

Three sensor models are compared, consisting of a single capacitor, a capacitor and resistor in series, and a capacitor and resistor in parallel. Among these, the series model provides the best fit, as indicated by the reduced χ^2 . The extracted series resistance in the sensor is likely due to contributions from the readout electronics or the depleted bulk.

In the second part, this model is applied to determine the capacitance of sensors with a thickness of 100 μm and 200 μm as a function of increasing bias voltage. For voltages below 136 V, both sensors show the same characteristics. In general, the capacitance follows the expected $1/\sqrt{V}$ characteristic, with the exception of a constant offset for bias voltages below 42 V. While there are several effects interfering with the accuracy of the measurements for low depletion depths, like the readout electronics and lateral depletion, these cannot describe the characteristic kink in the capacitance. The best explanation is given by the contact of two depletion regions, from the edge pixel and the isolation n-well. In the range of the full depletion, the capacitance of the thinner sensor deviates to lower values in comparison to the \sqrt{V} behaviour shown by the thicker sensor. In the same area, an abrupt increase in current is also visible in the IV curve. These two effects are caused by the depletion region reaching the damaged area on the backside of the sensor, which interfere with the electric field. At full depletion, the sensor capacitance stays constant with increasing voltage. For the area with the \sqrt{V} characteristic, a resistivity of $(405 \pm 8) \Omega\text{cm}$ is observed for the 200 μm thick sensor. The resistivity of the 100 μm thick sensor is determined to $(403 \pm 10) \Omega\text{cm}$. The corresponding doping concentration for the 200 μm thick sensor is $(3.21 \pm 0.06) \times 10^{13} \text{cm}^{-3}$ and for the 100 μm thick sensor it is $(3.22 \pm 0.07) \times 10^{13} \text{cm}^{-3}$.

Performing the same measurement for both sensors at lower temperatures shows that for the 200 μm thick sensor the temperature has no significant effect on the capacitance while for the thinner sensor, the temperature leads to lower capacitance values in the voltage range where the depletion reaches the damage layer on the backside [29]. As the current for the cooled measurement is low, this cannot be the only reason for the deviation. Here, the deviation is caused by the trapping of electrons in energy levels created by the defects. Due to the low thermal energy, the electrons cannot be detrapped from these traps and this manifests as a lower capacitance value. Further analysis of this effect lies beyond the scope of this thesis.

In the next part, sensors irradiated with non-ionizing radiation are investigated. The

capacitance measurements show that increasing irradiation results in lower capacitance values at the same bias voltage, indicating a reduced doping concentration. Such a decrease is expected, since irradiation displaces atoms from their lattice sites, thereby preventing dopant atoms from contributing as active dopants. The CV measurements of the irradiated sensors at room temperature do not exhibit the expected $1/\sqrt{V}$ -dependence, but instead the capacitance deviates towards slightly higher values. This deviation increases with both higher irradiation and higher bias voltage, indicating that leakage current and temperature influence the measurement. At lower temperatures, the capacitance decreases significantly and remains constant at a low value. This behaviour is similar to the effects of temperature on the damaged region of the 100 μm thick sensor. The damage caused by the irradiation induces intermediary energy levels which act as trapping centres for the electron. As the irradiation fluence increases, the density of such traps rises, making the effect more pronounced. Overall, the developed method provides a precise and versatile tool for HV-MAPS characterization, revealing clear dependencies of capacitance on temperature and irradiation.

10.2 Outlook

Within this thesis, a pronounced temperature dependence is observed for the irradiated MightyPix1 sensors. Since the sensor is intended to be cooled in the LHCb experiment, a better understanding of this effect is important. A key open question is whether the observed behaviour is specific to capacitance measurements or whether it also impacts the performance. First measurements indicate that the performance requirements of LHCb are fulfilled. Yet, further systematic measurements at different irradiation fluences and various temperatures have the potential to obtain more quantitative results for the capacitance measurement.

In addition to CV- and IV-measurements, further insight could be gained from dedicated comparisons of the difference in potential between the two biasing guard rings (so-called VV-curves). A combination of all three measurements could be insightful. Furthermore, the characteristic kink at low bias voltages could provide valuable information about the spreading of the depletion zone in the sensor bulk. To investigate this feature, measurements on sensors with different chip layouts and pixel geometries are required, complemented by dedicated TCAD simulations.

References

- [1] Peter W. Higgs. Broken symmetries and the masses of gauge bosons. *Phys. Rev. Lett.*, 13:508–509, Oct 1964.
- [2] S. Chatrchyan et al. Observation of a new boson at a mass of 125 gev with the cms experiment at the lhc. *Physics Letters B*, 716(1):30–61, 2012.
- [3] MissMJ. Standard model of elementary particles (antiparticles), 2006. Licensed under CC BY-SA 4.0.
- [4] LHCb Collaboration. LHCb VELO Upgrade Technical Design Report. Technical report, 2013.
- [5] Magnet Design Team and the LHCb Collaboration. LHCb magnet: Technical Design Report. CERN-LHCC report CERN-LHCC-2000-007 (LHCb-TDR-1), CERN, Geneva, 2000. Warm dipole magnet, integrated field 4Tm, max. B 1.2T.
- [6] Ya Zhao, Laurent Dufour, Wouter Hulsbergen, Zihan Gao, Blake Leverington, and Zehua Xu. Measurement of SciFi hit resolution at LHCb. Technical report, CERN, Geneva, 2025.
- [7] LHCb Collaboration. LHCb Tracker Upgrade Technical Design Report. Technical report, CERN, 2014.
- [8] LHCb Trigger and Online Upgrade Technical Design Report. Technical report, 2014.
- [9] Tim Gershon. Status of scoping document review and next steps. In *8th Workshop on LHCb Upgrade II*, Heidelberg, Germany, March 2025. Presented at Heidelberg University, March 26, 2025.
- [10] N. Harnew, R. Gao, T. Hadavizadeh, T.H. Hancock, J.C. Smallwood, N.H. Brook, S. Bhasin, D. Cussans, J. Rademacker, R. Forty, C. Frei, T. Gys, D. Piedigrossi, M.W.U. van Dijk, E.P.M. Gabriel, T. Conneely, J. Milnes, T. Blake, M.F. Cicala, T. Gershon, T. Jones, and M. Kreps. The torch time-of-flight detector. *Nuclear Instruments and Methods in Physics Research Section A: Accelerators, Spectrometers, Detectors and Associated Equipment*, 1048:167991, 2023.
- [11] LHCb. Framework TDR for the LHCb Upgrade II. Technical report, CERN, Geneva, 2021.
- [12] Hermann Kolanoski and Norbert Wermes. *Particle Detectors: Fundamentals and Applications*. Oxford University Press, 06 2020.
- [13] S. et al. Navas. Review of particle physics. *Phys. Rev. D*, 110:030001, Aug 2024.

- [14] National Institute of Standards and Technology. X-ray mass attenuation coefficients - table 1. <https://physics.nist.gov/PhysRefData/XrayMassCoef/tab1.html>, 2009. Accessed: 2025-06-26.
- [15] Claude Leroy and Pier-Giorgio Rancoita. *Silicon Solid State Devices and Radiation Detection*. World Scientific, 2012.
- [16] Simon M. Sze and Kwok K. Ng. *Physics of Semiconductor Devices*. John Wiley & Sons, 3rd edition, 2006.
- [17] Ben G. Streetman and Sanjay Banerjee. *Solid State Electronic Devices*. Pearson, 7 edition, 2016.
- [18] Helmuth Spieler. *Semiconductor detector systems*. Series on Semiconductor Science and Technology. Oxford University Press, Oxford, 2005.
- [19] Helmuth Spieler. Front-end electronics and signal processing. *AIP Conference Proceedings*, 680:20–25, 2003.
- [20] Günther Lutz. *Semiconductor Radiation Detectors*. Springer Berlin Heidelberg, 2007.
- [21] J. R. Srour and J. W. Palko. Displacement damage effects in irradiated semiconductor devices. *IEEE Transactions on Nuclear Science*, 60(3):1740–1766, 2013.
- [22] Michael Moll. *Radiation damage in silicon particle detectors: Microscopic defects and macroscopic properties*. PhD thesis, Hamburg U., 1999.
- [23] Jorge Jiménez-Sánchez, Pedro Blanco-Carmona, J. Hinojo, Rogelio Palomo, Rafael Millán, and F. Muñoz Chavero. Advanced system-on-chip field-programmable-gate-array-powered data acquisition system for pixel detectors. *Sensors*, 24:218, 12 2023.
- [24] Ivan Perić. A novel monolithic pixelated particle detector implemented in high-voltage cmos technology. *Nuclear Instruments and Methods in Physics Research Section A: Accelerators, Spectrometers, Detectors and Associated Equipment*, 582(3):876–885, 2007. VERTEX 2006.
- [25] S. Scherl. MightyPix1: A Novel High Voltage Monolithic Active Pixel Sensor for the proposed LHCb MightyTracker. 2023. Evaluation of prototype MightyPix1 before and after irradiation.
- [26] Wolfgang Demtroeder. *Experimentalphysik 2: Elektrizität und Optik*. Springer Spektrum, 5th edition, 2012.
- [27] N. Striebig and T. Frei. Mightypix documentation, 2025. Internal Note.

- [28] David Kuhn. Leakage currents in high voltage monolithic active pixel sensors in the context of the lhcb upgrade ii mightytracker. Bachelors thesis, Universität Heidelberg, 2025.
- [29] Anna Lelia Maria Fuchs. Development of a quality control procedure for mupix11 pixel sensors for the mu3e vertex detector. Bachelors thesis, Universität Heidelberg, 2023.
- [30] Matthew Lewis Franks. *Design and characterisation of High-Voltage CMOS (HV-CMOS) detectors for particle physics experiments*. The University of Liverpool (United Kingdom), 2022.
- [31] Johannes Gutenberg-Universität Mainz Institut für Kernchemie. Triga mark ii forschungsreaktor mainz. <https://www.kernchemie.uni-mainz.de/triga/>, 2025. Accessed: 2025-08-14.
- [32] N Croitoru, P.G Rancoita, M Rattaggi, G Rossi, and A Seidman. Influence of temperature on the i-v and c-v characteristics of si detectors irradiated at high fluences. *Nuclear Instruments and Methods in Physics Research Section A: Accelerators, Spectrometers, Detectors and Associated Equipment*, 388(3):340–344, 1997. Radiation Effects on Semiconductor Materials, Detectors and Devices.
- [33] Synopsys Inc. *Sentaurus TCAD*, XYZ. Version XYZ, <https://www.synopsys.com/silicon/tcad.html>.
- [34] Annie G. Meneses. *TCAD Simulations and Characterization of High-Voltage Monolithic Active Pixel Sensors*. Ph.d. thesis, Ruprecht-Karls-Universität Heidelberg, Physikalisches Institut, Heidelberg, Deutschland, 2023.

11 Appendix

.1 Silicon values

Quantity	value
Atomic number	14
Atomic mass	$M=28.0855 \text{ g mol}^{-1}$
Density	$\rho_{Si} = 2.329 \text{ g cm}^{-3}$
radiation length	$X_{0,Si} = 9.37 \text{ cm}$
Bandgap	$E_g = 1.12 \text{ eV}$

Table 4: Important properties for silicon.

.2 Impedance and Phase-shift Fits

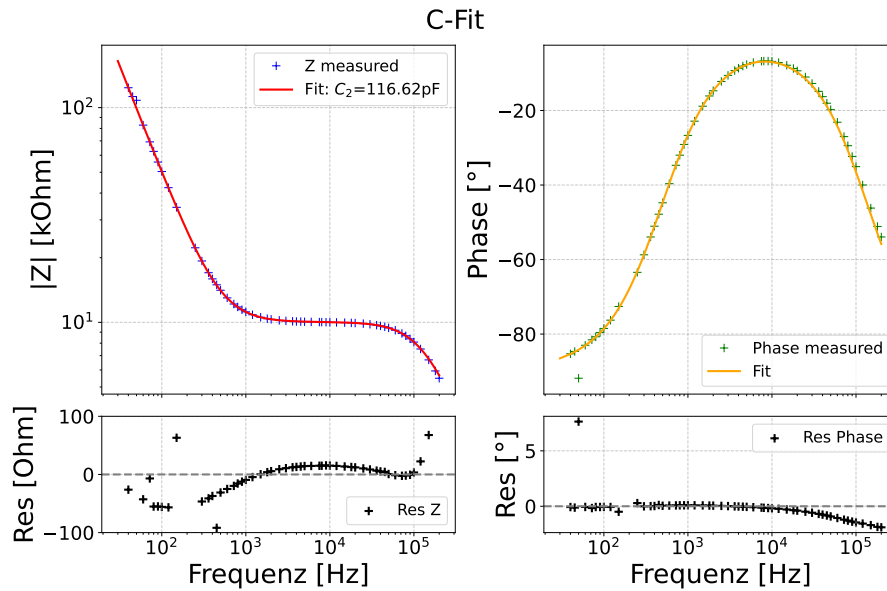


Figure 48: two-dimensional capacitance-fit with residuals for a 68 pF Capacitor

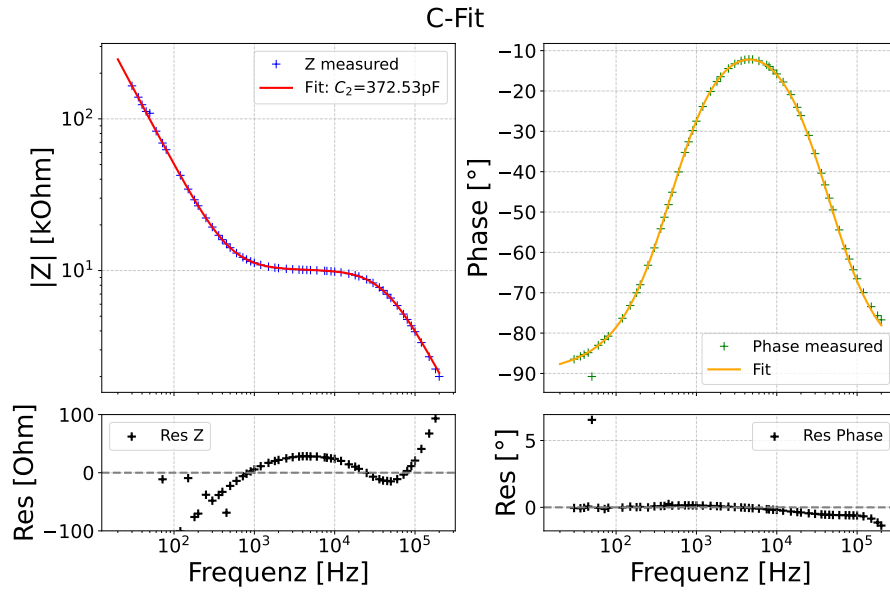


Figure 49: two-dimensional capacitance-fit with residuals for a 330 pF Capacitor

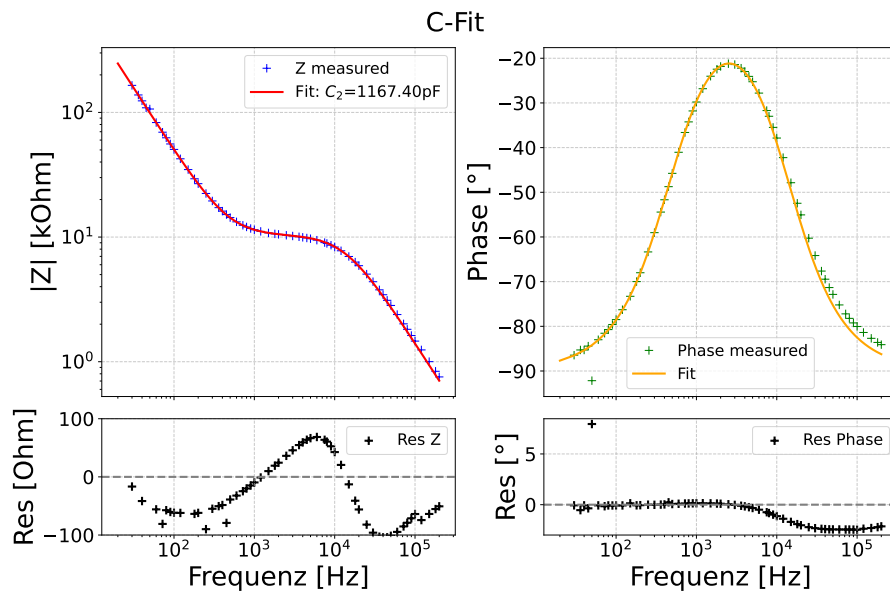


Figure 50: two-dimensional capacitance-fit with residuals for a 1.1 nF Capacitor

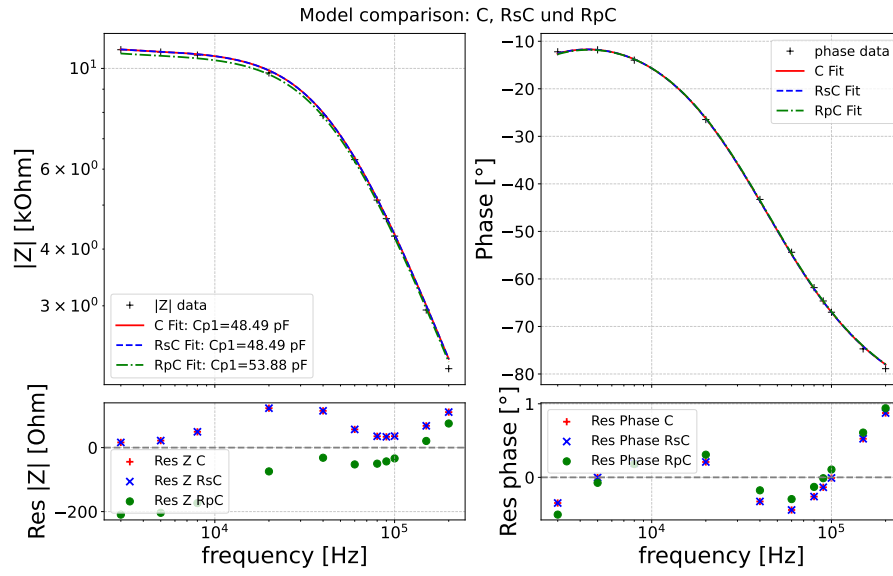
.3 Fit-Model Comparison at lower Temperatures

Figure 51: comparison of the three fit-models with residuals for the 4e14 sensor at a bias voltage of 120V

.4 Acknowledgments

First of all I would like to thank Prof. Dr. Ulrich Uwer for giving me the opportunity to work on this interesting research topic within the LHCb Heidelberg group. I am also thankful to Prof. Dr. Norbert Herrmann for kindly agreeing to serve as the second examiner of my thesis.

I would also like to sincerely thank Ruben and Sebastian for their supervision and for always being there to guide me and answer all of my questions.

I am deeply grateful to all proofreaders of my thesis: Ruben, who contributed extensively, Lucas, Celina, David, Benni and Heiko.

Additionally, I am thankful to all members of the LHCb Heidelberg group for making it pleasant to be there.

Thanks as well to my friends and family who supported me and for taking the time to proofread my work. Here I want to give a special thanks to Laura Hegeler for taking a lot of her time to proofread.

List of Figures

1	Overview of the elementary particles in the Standard Model, including fermions (quarks and leptons) and bosons (force carriers) [3].	7
2	Schematic of the LHCb detector[7].	9
3	Schematic front view of the proposed Mighty Tracker. The central region (pink/blue) feature high granularity HV-MAPS, while the outer section features Scintillating Fibres. [11]	10
4	Mean energy-loss by ionization as a function of $\beta\gamma$. [13]	12
5	Schematic energy-band structure of insulators (a), semiconductors (b) and conductors (c). E_G is the energy distance of the band gap [12]	15
6	Density of states, fermi dirac distribution and electron density for semiconductors	17
7	Schematic of the lattice in n-doped (a) and p-doped (b) silicon. [12]	19
8	Energy-levels with electron and hole drift for a p-n-junction. [12]	20
9	Different kinds of lattice defects in irradiated silicon. [12]	26
10	Location of intermediary energy levels in the bandgap, caused by substrate defects. [12]	26
11	Effects of annealing on the doping concentration of a high ohmic n-type substrate[22]	27
12	Schematic of Hybrid Pixel sensors (left) and monolithic pixel sensors (right) [23]	28
13	Working principle of an HV-MAPS [25].	29
14	Bode plot for RC-Circuits ($C=100\text{nF}$ and $R=1\text{k}\Omega$)	34
15	Close up Photo of the MightyPix1 glued onto the PCB used in this thesis. .	36
16	Measurement circuit used for the measurements in the thesis (a) and replacement circuit used for fitting (b).	37
17	breadboard with the circuit used for the measurements	38
18	Photo of the measurement setup in the laboratory.	38
19	Capacitor soldered onto a SMA-connector for the validation measurements. .	39
20	Two-dimensional capacitance-fit with residuals for a 470 pF Capacitor. . . .	40
21	Plot of the capacitance values obtained from the fit using the complete setup against those measured directly by the LCR metre. The y-intercept of the linear fit gives the stray capacitance.	41
22	voltage over time at the DUT for an AC signal with $f=300\text{Hz}$ and a bias voltage $V_{bias} = -10\text{V}$	41
23	Side view of a simplified HV-MAPS showing the chip guard ring and pixel guard ring contacts. The backside contact is connected to the bottom of the sensor, which is not included in this sketch.	42
24	Cooling Setup with dry ice used in this thesis.	43

25	IV-curve of the unirradiated 200 μm and 200 μm thick sensor	46
26	Comparison of the three fit-models with residuals for a bias voltage of –180 V. RsC refers to the serial model, RpC refers to the parallel model and C denotes the fit assuming a capacitor without resistor.	47
27	CV-curve for the 200 μm Sensor for all three models.	48
28	RV-curve for the 200 μm Sensor for the serial and parallel model.	49
29	IV-measurements of the 100 μm and 200 μm thick sensor at room tempera- ture. The green line indicates a bias voltage of –136 V and the red line of –168 V.	50
30	CV-curves for the 100 μm and 200 μm thick sensor at 23 °C.	51
31	Calculated depletion of the 100 μm and 200 μm thick sensor.	51
32	Resistivity and doping concentration for the 100 μm and 200 μm sensor cal- culated using the assumption of a plate capacitor	52
33	IV-measurements for the 100 μm and 200 μm sensors in cooled conditions and at room temperature as reference.	53
34	CV-measurements for the 200 μm sensors in cooled conditions and at room temperature as reference.	54
35	CV-measurements for the 100 μm sensors in cooled conditions and at room temperature as reference.	54
36	IV-measurements for the $1 \times 10^{13} \text{ n}_{\text{eq}}/\text{cm}^2$ (in green) and $5 \times 10^{13} \text{ n}_{\text{eq}}/\text{cm}^2$ (in blue) irradiated sensors at room temperature and at approximately –20 °C.	57
37	CV-curves for the $5 \times 10^{13} \text{ n}_{\text{eq}}/\text{cm}^2$ irradiated sensor at three different tem- peratures	58
38	CV-curves for the $1 \times 10^{14} \text{ n}_{\text{eq}}/\text{cm}^2$ irradiated sensor at three different tem- peratures	59
39	CV-measurements for all irradiates sensors at room temperature. For a better comparison, the capacitance for the unirradiated sensor is also shown.	59
40	Calculated depletion depth for all irradiates sensors at room temperature.	60
41	Calculated doping concentration for all irradiates sensors at room temper- ature.	61
42	CV-curves for different sensors which all show an offset at low voltage.	63
43	depletion depth for different sensors which all show an offset at low voltage.	64
44	Side view TCAD simulation of the depletion in an HV-MAPS at low bias voltage. The depletion is depicted by the white lines. The space charge values do not correspond to the MightyPix1. [34]	65
45	Schematic of a silicon drift detector. [12]	66
46	CV-curve of a silicon drift detector. [12]	66
47	Schematic side-view of the MightyPix1 with the characteristic distance of 40 μm from the isolation n-well to the CGR and the edge pixel.	67
48	two-dimensional capacitance-fit with residuals for a 68 pF Capacitor	75

49	two-dimensional capacitance-fit with residuals for a 330 pF Capacitor . . .	76
50	two-dimensional capacitance-fit with residuals for a 1.1 nF Capacitor . . .	76
51	comparison of the three fit-models with residuals for the 4e14 sensor at a bias voltage of 120V	77

List of Tables

1	Table of the most important properties of the MightyPix1 [27].	35
2	Comparison of the capacitance values obtained from the fit using the complete setup with those measured directly by the LCR metre. ΔC is the difference between the two values.	40
3	Fitted Capacitance for the different models with the reduced χ^2 . RsC refers to the serial model, RpC refers to the parallel model and C denotes the fit assuming a capacitor without resistor.	48
4	Important properties for silicon.	75

Hilfsmittel

Für Berechnungen, Datenanalyse und Textunterstützung wurden folgende Hilfsmittel verwendet:

- Python 3
- WolframAlpha
- DeepL (für Textvorschläge)
- ChatGPT (für Coding-Vorschläge)

Erklärung

Ich versichere, dass ich diese Arbeit selbstständig verfasst und keine anderen als die angegebenen Quellen und Hilfsmittel benutzt habe.

Heidelberg, den 17.08.2025,

Ian David Linnett